The community Noah land surface model with multiparameterization options (Noah-MP): 1. Model description and evaluation with local-scale measurements

Guo-Yue Niu,[1,2] Zong-Liang Yang,[1] Kenneth E. Mitchell,[3] Fei Chen,[4] Michael B. Ek,[3] Michael Barlage,[4] Anil Kumar,[5] Kevin Manning,[4] Dev Niyogi,[6] Enrique Rosero,[1,7] Mukul Tewari,[4] and Youlong Xia[3]

Received 4 October 2010; revised 3 February 2011; accepted 27 March 2011; published 24 June 2011.

[1] This first paper of the two-part series describes the objectives of the community efforts in improving the Noah land surface model (LSM), documents, through mathematical formulations, the augmented conceptual realism in biophysical and hydrological processes, and introduces a framework for multiple options to parameterize selected processes (Noah-MP). The Noah-MP's performance is evaluated at various local sites using high temporal frequency data sets, and results show the advantages of using multiple optional schemes to interpret the differences in modeling simulations. The second paper focuses on ensemble evaluations with long-term regional (basin) and global scale data sets. The enhanced conceptual realism includes (1) the vegetation canopy energy balance, (2) the layered snowpack, (3) frozen soil and infiltration, (4) soil moisture-groundwater interaction and related runoff production, and (5) vegetation phenology. Sample local-scale validations are conducted over the First International Satellite Land Surface Climatology Project (ISLSCP) Field Experiment (FIFE) site, the W3 catchment of Sleepers River, Vermont, and a French snow observation site. Noah-MP shows apparent improvements in reproducing surface fluxes, skin temperature over dry periods, snow water equivalent (SWE), snow depth, and runoff over Noah LSM version 3.0. Noah-MP improves the SWE simulations due to more accurate simulations of the diurnal variations of the snow skin temperature, which is critical for computing available energy for melting. Noah-MP also improves the simulation of runoff peaks and timing by introducing a more permeable frozen soil and more accurate simulation of snowmelt. We also demonstrate that Noah-MP is an effective research tool by which modeling results for a given process can be interpreted through multiple optional parameterization schemes in the same model framework.

Citation: Niu, G.-Y., et al. (2011), The community Noah land surface model with multiparameterization options (Noah-MP): 1. Model description and evaluation with local-scale measurements, *J. Geophys. Res.*, *116*, D12109, doi:10.1029/2010JD015139.

1. Introduction

[2] Land can remember weather events or climate anomalies through variations in its heat and water storages. In turn, land heat and water storage anomalies (the filtered signals of noisy weather events) can affect climate predictability through their effects on surface energy and water fluxes [*Roesch et al.*, 2001; *Jiang et al.*, 2009, and references therein]. For instance, anomalous heat storage due to anomalous snow accumulation in winter can affect the warming in spring or early summer through melting. Anomalous water stored in reservoirs (snowpack, soil, and aquifer) during wet seasons can feed back to the atmosphere through evapotranspiration (ET) in subsequent dry seasons; this effect can be more efficient in vegetated areas through plant stomata and root uptakes of soil water. Soil water anomalies can persist from weeks to seasons [*Pielke et al.*, 1999; *Schlosser and Milly*, 2002] and affect climate predictability through the

[1]Department of Geological Sciences, John A. and Katherine G. Jackson School of Geosciences, University of Texas at Austin, Austin, Texas, USA.
[2]Biosphere 2, University of Arizona, Tucson, Arizona, USA.
[3]Environmental Modeling Center, National Centers for Environmental Prediction, National Oceanic and Atmospheric Administration-National Weather Service, Camp Springs, Maryland, USA.
[4]Research Applications Laboratory, National Center for Atmospheric Research, Boulder, Colorado, USA.
[5]Hydrological Science Branch, NASA Goddard Space Flight Center, Greenbelt, Maryland, USA.
[6]Departments of Agronomy and Earth and Atmospheric Sciences, Purdue University, West Lafayette, Indiana, USA.
[7]Now at ExxonMobil Upstream Research Company, Houston, Texas, USA.

0148-0227/11/2010JD015139

response of vegetation and associated ET, most significantly in dry-to-wet transition regions [*Koster et al.*, 2004; *Guo et al.*, 2006]. However, representations of land heat and water storages and their relationships with fluxes are still problematic in land surface models (LSMs) [*Dirmeyer et al.*, 2006a]. Through analyses of the Global Land-Atmosphere Coupling Experiment (GLACE) [*Koster et al.*, 2006] model simulations, *Dirmeyer et al.* [2006a] showed that no individual model adequately represented soil water and latent heat and their relationship, but that the multimodel average had the best performance. This indicated a necessity for further improvement of LSMs and validation against observational data sets.

[3] Through three decades of development, LSMs have become more comprehensive and evolving to the third generation to represent an increasing number of interactions and feedbacks between physical, biological, and chemical processes [*Sellers et al.*, 1997; *Pitman*, 2003; *Yang*, 2004]. For instance, snow submodels have evolved from simple bulk-layer models to multilayer models to accommodate more physical processes [*Jin et al.*, 1999; *Dai et al.*, 2003; *Xue et al.*, 2003; *Yang and Niu*, 2003; K. M. Andreadis and D. P. Lettenmaier, Implications of representing snowpack stratigraphy for large-scale passive microwave remote sensing, submitted to *Journal of Geophysical Research*, 2011] and included the effects of vegetation on snow surface energy and mass balance [e.g., *Essery et al.*, 2003; *Niu and Yang*, 2004]. Soil hydrology schemes have included the exchange of water between an unconfined aquifer and the overlying soil column [*Liang et al.*, 2003; *Yeh and Eltahir*, 2005; *Maxwell and Miller*, 2005; *Niu et al.*, 2007] and the effects of lateral transport of groundwater on redistribution of soil moisture at a finer scale [*Fan et al.*, 2007; *Maxwell and Kollet*, 2008]. Runoff schemes have considered the effects of subgrid topography on soil water distribution and runoff generation [e.g., *Famiglietti and Wood*, 1994; *Koster et al.*, 2000; *Chen and Kumar*, 2001; *Niu et al.*, 2005] following the concepts of TOPMODEL [*Beven and Kirkby*, 1979; *Sivapalan et al.*, 1987]. Additionally, LSMs have introduced vegetation dynamics by explicitly considering plant photosynthesis, respiration, and related nitrogen cycle [e.g., *Sellers et al.*, 1996; *Bonan*, 1996; *Dickinson et al.*, 1998, 2002]. Despite these efforts, no models participating in GLACE [*Koster et al.*, 2006] implemented all the above mentioned parameterization schemes.

[4] However, it is questionable whether augmenting an LSM with a single combination of as many new parameterizations as possible would improve its performance. The reason for this concern is threefold. First, any parameterization scheme of a complex process is an approximation which is always limited by our incomplete understanding of the process that is hampered by limited data. For example, it is impossible to test a parameterization scheme for soil water stress on the plant stomata resistance against all soil, vegetation, and climate conditions. Second, choosing a parameterization scheme for use in a given LSM is sometimes arbitrary, and possibly the selected scheme may not be compatible with other schemes in the LSM. Third, the compatibility may be further degraded due to the interactions of parameters in the newly introduced scheme with those in other schemes of the LSM [*Rosero et al.*, 2009].

[5] It is promising that multimodel averages resulted in generally better behavior as demonstrated in various offline phases of the Project for Intercomparison of Land Surface Parameterization Schemes (PIPLS) and two phases of the Global Soil Wetness Project (GSWP) [*Entin et al.*, 1999; *Guo and Dirmeyer*, 2006; *Dirmeyer et al.*, 2006b] and online (coupled to atmospheric models) in GLACE [*Dirmeyer et al.*, 2006a]. This indicates that an LSM with multiphysics options offers potential to mimic multimodel behaviors and is well suited to conduct ensemble model simulations. For the atmospheric models, ensemble simulations using multiple cumulus parameterization schemes [*Grell and Dévényi*, 2002] have been demonstrated to provide better climate prediction [*Liang et al.*, 2007]. Hydrologists have been pursuing multimodel ensemble streamflow predictions [*Georgakakos et al.*, 2004; *Duan et al.*, 2007].

[6] Therefore, it is necessary to develop an LSM that accommodates numerous combinations of parameterization schemes for an ensemble representation of processes in nature. The chameleon land surface model (CHASM) [*Desborough*, 1999; *Pitman et al.*, 2003] was among the earliest efforts to explore the impact of model complexity on model performance. Different from CHASM, the model designed in this paper focuses on various parameterization schemes at almost the same level of complexity.

[7] We select the widely used Noah LSM as our baseline model because it is coupled with the Weather Research and Forecast (WRF) model that provides multioptions for atmospheric physical processes. The Noah LSM is known to have biases in simulating runoff and snowmelt [*Bowling et al.*, 2003; *Slater et al.*, 2007]. Thus, we first augment its representations of hydrological processes and surface energy fluxes that affect the hydrological processes. The Noah LSM has a combined surface layer of vegetation and snow (when snow covers the soil surface), impeding an accurate prediction of snow skin temperature and thus snowmelt. Therefore, we first separated the vegetation canopy from the ground and then added various hydrological schemes. The augmentations are complex and comprehensive including the structural change. To facilitate interpreting differences in the modeling results between the evolutional versions and the original Noah LSM, we retained most of the schemes of the Noah LSM and then design multiparameterization options (Noah-MP) for selected processes. These selected processes in Noah-MP are now limited to the key processes that are already represented in the Noah LSM, although other processes may be important for the model's overall performance and subject to addition in future model developments. The model with multiple parameterization options has a great potential to facilitate (1) physically based ensemble climate predictions, (2) identification of the optimal combinations of schemes and explanation of model differences, and (3) identification of critical processes controlling the coupling strength [*Koster et al.*, 2006] between the land surface and the atmosphere.

[8] This first paper of the two-part series is organized as follows. Section 2 briefly introduces the major features of a recent version of Noah LSM (version 3.0) and its major flaws in simulating snow and subsurface hydrology. Section 3 describes major augmentations to various parameterization schemes. Section 4 introduces a framework for multiple parameterization options. Section 5 presents the testing

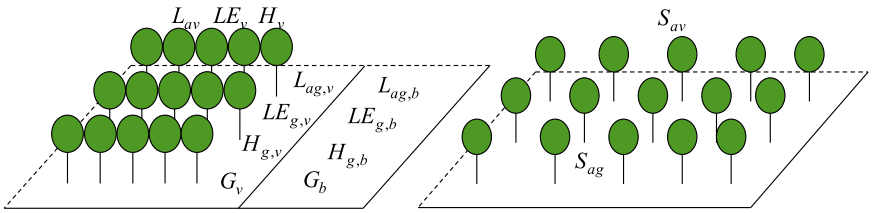

Figure 1. Schematic diagram for the "semitile" subgrid scheme. (left) Net longwave (L_a), latent heat (LE), sensible heat (H), and ground heat (G) fluxes are computed separately for bare soil (subscript "b") and vegetated (subscript "v") tiles following the "tile" approach, while (right) short-wave radiation fluxes (S_{av} and S_{ag}) are computed over the entire grid cell considering gap probabilities.

results and sensitivity tests with different options at some local sites. The second paper presents the testing results over global river basins mainly at monthly time scale and an ensemble simulation of 36 members (36 models) [*Yang et al.*, 2011].

2. The Baseline Noah Land Surface Model

[9] The Noah LSM has a long history of development through multiinstitutional cooperation [*Mahrt and Ek*, 1984; *Mahrt and Pan*, 1984; *Pan and Mahrt*, 1987; *Chen et al.*, 1996; *Schaake et al.*, 1996; *Chen et al.*, 1997; *Koren et al.*, 1999; *Ek et al.*, 2003] and has been widely used by the National Centers for Environmental Prediction (NCEP) in operational weather and climate predictions, by the Weather Research Forecast (WRF) model community, and by the Air Force Weather Agency. The development efforts have improved the model performance in both offline [*Mitchell et al.*, 2004; *Chen et al.*, 2007] and coupled modes [*Ek et al.*, 2003].

[10] Noah version 3.0 (V3) has a combined surface layer of vegetation and soil surface, over which surface energy fluxes are computed. Such a model structure impedes its further development as a process-based dynamic leaf model, because it cannot explicitly compute photosynthetically active radiation (PAR), canopy temperature, and related energy, water, and carbon fluxes. Noah has a bulk layer of snow and soil. For a thick snowpack, such a layer structure tends to underestimate the ground heat flux because of the combined thickness of snowpack and half of the top-layer soil, leaving too much energy at the snow surface and being thus too prone to snowmelt. Additionally, percolation, retention, and refreezing of melt liquid water cannot be readily represented in such a layer structure. Noah has a total soil depth of two meters and uses gravitational free drainage at the model bottom as the lower boundary condition of soil moisture. Drained water from the 2 m soil bottom should accumulate in its underlying soil or aquifer during wet seasons when recharge rate exceeds discharge rate and, driven by capillary forces, be able to be drawn back to the 2 m soil column in dry seasons. Noah's shallow soil column is not able to capture the critical zone (down to 5 m) to which the surface energy budgets are most sensitive [*Kollet and Maxwell*, 2008]; immediate removal of the drained water (due to the free drainage scheme) in Noah may result in too short memories of antecedent weather events or climate anomalies. The impeding effect of frozen soil on infiltration and further effects on river discharge is evidently weaker [e.g., *Shanley and Chalmers*, 1999; *Lindström et al.*, 2002] than that represented in most LSMs. The frozen soil in Noah is too impervious under most vegetation and climate conditions, resulting in too much surface runoff in spring or early summer and, hence, less infiltration of snowmelt water into soil.

3. Augmentations to the Noah LSM

[11] To solve the above mentioned problems, we first introduced (1) a vegetation canopy layer to compute the canopy and the ground surface temperatures separately, (2) a modified two-stream radiation transfer scheme [*Yang and Friedl*, 2003; *Niu and Yang*, 2004] considering canopy gaps to compute fractions of sunlit and shaded leaves and their absorbed solar radiation, (3) a Ball-Berry type stomatal resistance scheme [*Ball et al.*, 1987; *Collatz et al.*, 1991, 1992; *Sellers et al.*, 1996; *Bonan*, 1996] that relates stomatal resistance to photosynthesis of sunlit and shaded leaves, and (4) a short-term dynamic vegetation model [*Dickinson et al.*, 1998]. We also implemented in Noah a simple groundwater model with a TOPMODEL-based runoff scheme [*Niu et al.*, 2005, 2007], a physically based three-layer snow model [*Yang and Niu*, 2003], and a frozen soil scheme that produces a greater soil permeability [*Niu and Yang*, 2006] into Noah. The design of the augmented Noah largely solves the above mentioned problems and enables the choice of multiple, alternative options for each physical process.

3.1. Surface Energy Balance

[12] We separated the canopy layer from the ground surface and introduced a "semitile" subgrid scheme to represent land surface heterogeneity (Figure 1). In the semitile scheme, shortwave radiation transfer is computed over the entire grid cell considering gap probabilities, while longwave radiation, latent heat, sensible heat, and ground heat fluxes are computed separately over two tiles: a fractional vegetated area (F_{veg}) and a fractional bare ground area ($1 - F_{veg}$). The conventional tile or "mosaic" method assembles vegetation canopies within a grid cell according to satellite-derived vegetation distribution data that are estimated assuming the sun is overhead regardless of vegetation locations [*Koster and Suarez*, 1992], and thus it would overlap too many shadows whenever the sun is not overhead. As a result, it exposes too much ground surface covered by either short grass or snow, to solar radiation independent of the solar zenith angle (SZA). The semitile scheme is designed to (1) avoid such overlapping of shadows and (2) take advantage

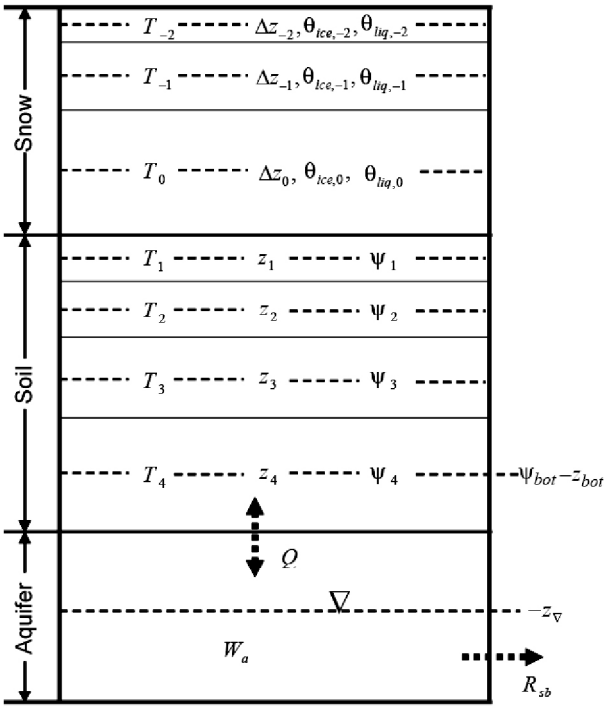

Figure 2. Schematic diagram for snow, soil, and an unconfined aquifer as represented in the model. The indices for the snow layers from the top are −2, −1, and 0 to continuously transition to soil layer's indices 1, 2, 3, and 4. The variables are described in detail in the text.

of the tile method in dealing with the nonlinear relationships between parameters and fluxes over vegetated and bare fractions.

[13] The semitile scheme first computes shortwave radiation transfer over a grid cell using a modified two-stream approximation assuming that the vegetation canopies are evenly distributed over a grid cell (Figure 1). The two-stream radiation scheme [*Dickinson*, 1983; *Sellers*, 1985] computes SZA-dependent fluxes that are reflected by the surface, absorbed by the canopy, and absorbed by the ground over two wave bands: visible and near-infrared. The scheme accounts for scattering and multiple reflections by the canopy and ground in two mainstreams of radiative fluxes: vertical upward and downward. However, it assumes that the canopy leaves are evenly distributed within a grid cell. The modified two-stream scheme [*Yang and Friedl*, 2003; *Niu and Yang*, 2004] accounts for aggregation of the evenly distributed leaves into canopy crowns with between-canopy and within-canopy gaps (as shown in Figure 1), which vary with radius and thickness of the canopy, tree density (the distance between trunks), and SZA.

[14] The canopy-absorbed solar radiation over a grid cell (S_{av}) heats the vegetation canopy over the fractional vegetated area (F_{veg}), and the vegetation canopy emits longwave radiation to the atmosphere and exchanges latent (LE_v) and sensible (H_v) heat with the canopy air at a temperature (T_v) that satisfies the balance of the energy budgets:

$$S_{av} = F_{veg}(L_{av}(T_v) + LE_v(T_v) + H_v(T_v)) \quad (1)$$

where L_{av} is net longwave radiation (positive upward) absorbed by the vegetation canopy, and LE_v includes latent heat fluxes from transpiration through stomata and evaporation of the canopy intercepted water.

[15] The ground-absorbed solar radiation over the grid cell, S_{ag}, is shared by the vegetated ground with an amount of $S_{ag}F_{veg}$ and the bare ground with an amount of $S_{ag}(1-F_{veg})$. The vegetated ground emits longwave radiation to the canopy and exchanges latent heat ($LE_{g,v}$) and sensible heat ($H_{g,v}$) fluxes with the canopy air and ground heat with the upper soil (G_v) at a temperature, $T_{g,v}$ that satisfies the balance of the energy budgets:

$$F_{veg}S_{ag} = F_{veg}\left(L_{ag,v}\left(T_{g,v}\right) + LE_{g,v}\left(T_{g,v}\right) + H_{g,v}\left(T_{g,v}\right) + G_v\left(T_{g,v}\right)\right) \quad (2)$$

where $L_{ag,v}$ is the net longwave radiation (positive upward) absorbed by the vegetated ground. Analogously, the bare ground at the fractional area, $1-F_{veg}$, emits longwave radiation to the atmosphere and exchanges latent heat ($LE_{g,b}$) and sensible heat ($H_{g,b}$) with the atmosphere at a temperature $T_{g,b}$ that satisfies the balance of the energy budgets:

$$\begin{aligned}\left(1-F_{veg}\right)S_{ag} = \left(1-F_{veg}\right)&\left(L_{ag,b}\left(T_{g,b}\right)\right.\\ &\left.+LE_{g,b}\left(T_{g,b}\right) + H_{g,b}\left(T_{g,b}\right) + G_b\left(T_{g,b}\right)\right)\end{aligned} \quad (3)$$

where $L_{ag,b}$ is the net longwave radiation (positive upward) absorbed by the bare ground fraction, and G_b is the ground heat flux in the bare ground fraction.

[16] The net longwave radiation (L_a), latent heat (LE), sensible heat (H), and ground heat (G) fluxes of a model grid cell are, respectively,

$$\begin{aligned} L_a &= \left(1-F_{veg}\right)L_{ag,b} + F_{veg}\left(L_{av}+L_{ag,v}\right)\\ LE &= \left(1-F_{veg}\right)LE_{g,b} + F_{veg}\left(LE_v+LE_{g,v}\right)\\ H &= \left(1-F_{veg}\right)H_{g,b} + F_{veg}\left(H_v+H_{g,v}\right)\\ G &= \left(1-F_{veg}\right)G_b + F_{veg}G_v \end{aligned} \quad (4)$$

The surface energy balance equation over a grid cell is: $S_{av} + S_{ag} = L_a + LE + H + G$. The vegetation canopy temperature (T_v), ground surface temperature ($T_{g,v}$) in the vegetated fraction, and ground surface temperature in the bare fraction ($T_{g,b}$) are solved iteratively through equations (1)–(3). The energy fluxes in equations (1)–(4) are described in detail in Appendix A.

3.2. Snow and Frozen Soil

[17] On top of the four layer (4–L) soil structure, the snowpack can be divided by up to three layers depending on the total snow depth h_{sno} (see Figure 2), as shown by *Yang and Niu* [2003]. When $h_{sno} < 0.045$ m, no snow layer exists and the snowpack is combined with the topsoil layer. When $h_{sno} \geq 0.045$ m, the first snow layer is created with a layer thickness $\Delta z_0 = h_{sno}$ m. When $h_{sno} \geq 0.05$ m, two snow layers are created with $\Delta z_{-1} = \Delta z_0 = h_{sno}/2$ m. When $h_{sno} \geq 0.1$ m, the two-layer thicknesses are: $\Delta z_{-1} = 0.05$ m and $\Delta z_0 = (h_{sno} - \Delta z_{-1})$m. When $h_{sno} \geq 0.15$ m, a third layer is created; the three layer thicknesses are: $\Delta z_{-2} = 0.05$ m and $\Delta z_{-1} = \Delta z_0 = (h_{sno} - \Delta z_0)/2$ m. When $h_{sno} \geq 0.45$ m, the layer thicknesses for the three snow layers are: $\Delta z_{-2} =$

0.05 m, Δz_{-1} = 0.2 m, and $\Delta z_0 = (h_{sno} - \Delta z_{-2} - \Delta z_{-1})$ m. If a layer thickness is less than its minimum value (0.045 m, 0.05 m, and 0.2 m for the three layers from top to bottom) due to sublimation and/or melt, the layer is combined with its lower neighboring layer; the layers are then redivided depending on the total snow depth following the above procedure. The thinner first snow layer is designed to more accurately resolve the ground heat flux. The value of 0.045 m results from calibration against the diurnal variations of snow skin temperature observed at a French site (see Figure 7).

[18] Snow skin temperatures in the vegetated fraction ($T_{g,v}$) and bare fraction ($T_{g,b}$) are solved iteratively through the energy balance equations (2) and (3), respectively. G is regarded as the upper boundary condition of the snow/soil temperature equation, or the external forcing for changes in the heat storage of snow and soil. The temperatures of the snow and soil layers are then solved together through one tridiagonal matrix with its dimension varying with the total number of snow and soil layers.

[19] Snow and soil layer temperatures are then used to assess the energy for melting or freezing ($H_{m,i}$) for the ith snow and soil layers, i.e., the energy excess or deficit needed to change a snow or soil layer temperature to the freezing point T_{frz}:

$$H_{m,i} = C_i \Delta z_i \frac{T_i^{N+1} - T_{frz}}{\Delta t} \quad i = isno + 1, 4 \tag{5}$$

where T_i^{N+1} is the ith layer snow or soil temperature solved through the tridiagonal matrix (T_i^{N+1} can be greater than T_{frz} during midday hours in the melting season before the treatment of phase change). Δz_i and Δt are layer thickness and time step. Subscript "$isno$" represents the total number of snow layers in a negative number (for instance, when there are three snow layers, $isno = -3$; $isno+1 = -2$ represents the surface snow layer). C_i is the volumetric heat capacity:

$$C_i = \begin{cases} C_{ice}\theta_{ice,i} + C_{liq}\theta_{liq,i} & i = isno + 1, 0 \\ C_{ice}\theta_{ice,i} + C_{liq}\theta_{liq,i} + C_{soil}(1 - \theta_{sat}) & i = 1, 4 \end{cases} \tag{6}$$

where $\theta_{ice,i}$ and $\theta_{liq,i}$ stand for partial volume of ice and liquid water in the ith snow or soil layer (Figure 2), and C_{ice} and C_{liq} for volumetric heat capacity for ice and liquid water, respectively. θ_{sat} is soil porosity, and C_{soil} is the volumetric heat capacity of soil particles.

[20] When a snow or soil layer's ice content $\theta_{ice,i} > 0$ and $T_i^{N+1} > T_{frz}$, melting occurs. In the melting phase, H_m (>0) is limited by the latent heat consumed for melting all the ice in a layer within a time step, $L_f \theta_{ice,i} \rho_{ice} \Delta z_i / \Delta t$, where L_f and ρ_{ice} are latent heat of fusion (= 0.3336 × 10^6 J kg^{-1}) and ice density (= 917 kg m^{-3}). The $\theta_{liq,i}$ is limited by its maximum value of a snow layer (or holding capacity, $\theta_{liq\max,i}$ = 0.03 m^3/m^3); excessive $\theta_{liq,i}$ above $\theta_{liq\max,i}$ flows down to its lower neighboring layer and eventually to the soil surface. When $T_i^{N+1} < T_{frz}$ and liquid content $\theta_{liq,i} > 0$ (for snow) or $\theta_{liq,i} > \theta_{liq\max,i}$ (for soil), where $\theta_{liq,\max,i}$ is the upper limit of the supercooled liquid water (see section 4.6 for details), freezing occurs. The freezing energy H_m (<0) is limited by the latent heat released by freezing all the liquid water in a snow layer or the liquid water over $\theta_{liq,\max,i}$ in a soil layer within one time step. The residual energy that may not be consumed by melting or released from freezing is used to heat or cool the snow or soil layer.

[21] Snow density (or snow depth) is predicted, following *Anderson* [1976], by accounting for destructive or equi-temperature metamorphism, compaction due to the weight of the overlying layers of snow, and melt metamorphism. Because the third layer is very thick for a thick snowpack, the compaction due to its own weight is also taken into account following *Sun et al.* [1999].

[22] We further implemented a snow interception model [*Niu and Yang*, 2004] into the Noah model. Because the interception capacity for snowfall is much greater than that for rainfall, interception of snowfall by the canopy and subsequent sublimation from the canopy snow may greatly reduce the snow mass on the ground. The model allows for both liquid water and ice to be present on the vegetation canopy. The model accounts for loading and unloading of snowfall, melting of intercepted snow and refreezing of the meltwater, frost/sublimation, and dew/evaporation. The loading rate depends on snowfall rate and the maximum loading capacity, which is a function of leaf area index (LAI) and falling snow density following *Hedstrom and Pomeroy* [1998]. The unloading rate depends on wind speed and canopy temperature following *Roesch et al.* [2001]. Melting or freezing is assessed through the vegetation canopy temperature [*Niu and Yang*, 2004]. Stability correction to the undercanopy turbulent transfer is also introduced to account for the strong stable condition of the warmer canopy overlying the snow surface during the melting season. *Niu and Yang* [2004] demonstrated that properly representing these processes can improve the simulation of surface albedo, diurnal variations of canopy temperature, and heat exchanges between the canopy air and the underlying snow over boreal forest regions.

[23] The snow cover fraction (SCF) on the ground, $f_{sno,g}$, is parameterized as a function of snow depth, ground roughness length, and snow density following *Niu and Yang* [2007]. The scheme represents countless curves of SCF against snow depth corresponding to varying snow density during a snow season. It can result in a higher SCF during snowfall periods (with low snow densities) than in snowmelt periods (with high snow densities) with the same snow depth. The ground surface albedo, α_g, is then parameterized as an area-weighted average of albedos of snow (α_{sno}) and bare soil (α_{soi}): $\alpha_g = (1 - f_{sno,g})\,\alpha_{soi} + f_{sno,g}\,\alpha_{sno}$. The SCF of the canopy ($f_{sno,c}$) adopts the formulation of *Deardorff* [1978] for the wetted fraction of the canopy, depending on snow mass on the canopy. It is used as a weight to average the scattering parameters used in the two-stream approximation over fractional snow covered canopy ($f_{sno,c}$) and noncovered canopy ($1-f_{sno,c}$).

3.3. Groundwater

[24] Below the 2 m bottom of the Noah soil column, we added an unconfined aquifer to account for the exchange of water between the soil and the aquifer (Figure 2). Following *Niu et al.* [2007], the temporal variation in water stored in the aquifer is determined by the residual of recharge rate, Q,

minus discharge rate (base flow or subsurface runoff), R_{sb}. Q is then parameterized following Darcy's law and is positive when water enters the aquifer:

$$Q = -K_{bot}\frac{-z_{\nabla} - (f_{mic}\psi_{bot} - z_{bot})}{z_{\nabla} - z_{bot}} \quad (7)$$

where z_{∇} is the water table depth, ψ_{bot} and K_{bot} are the matric potential and hydraulic conductivity of the bottom soil layer, respectively, and z_{bot} (1.5 m in Noah) is the midpoint of the bottom soil layer. Note that we use K_{bot} not K_a, the hydraulic conductivity of the aquifer in the work by *Niu et al.* [2007] in the above equation for two reasons: (1) to avoid uncertainties in determining K_a because of the limited information about deep soil and aquifers and (2) to conveniently reduce the above equation to free drainage conditions. Additionally, we introduce a new parameter f_{mic}, the fraction of micropore content in the bottom-layer soil, to limit the upward flow (depending on the level of structural soil), with f_{mic} ranging from 0.0 to 1.0. When f_{mic} = 0.0 (structural soil or aquifers without micropores), equation (7) is then reduced to free drainage ($Q = K_{bot}$). When f_{mic} = 1.0 (textural soil full of micropores), $Q = K_{bot}\left(1 + \frac{\psi_{bot}}{z_{\nabla} - z_{bot}}\right)$, representing a maximum effect of groundwater on soil moisture. Equation (7) can be also interpreted as a model grid cell having a fractional area $(1 - f_{mic})$ with free drainage and a fractional area (f_{mic}) with a maximum effect of groundwater. The mean state and variability of soil moisture are very sensitive to the magnitude of f_{mic}; generally, a larger f_{mic} produces a wetter soil with a smaller soil moisture variability. Details on other aspects of the model, such as how to derive water table depth, are given by *Niu et al.* [2007].

3.4. Runoff

[25] We use a simple TOPMODEL-based runoff model [*Niu et al.*, 2005] to compute surface runoff and groundwater discharge, which are both parameterized as exponential functions of the depth to water table. Surface runoff is mainly saturation-excess (Dunne) runoff, i.e., the water (sum of rainfall, dew, and snowmelt) incident on the fractional saturated area of a model grid cell. The fractional saturated area, F_{sat}, is parameterized as:

$$F_{sat} = \left(1 - F_{frz}\right)F_{\max}e^{-0.5f\left(z_{\nabla} - z'_{bot}\right)} + F_{frz} \quad (8)$$

where $F_{\max}$ is the sum of fractional lowland areas where the land surface is inundated with water when the grid cell mean water table depth is zero. $F_{\max}$ can be derived from high-resolution subgrid topography (e.g., 30 m) of a model grid cell (e.g., 1° resolution) following TOPMODEL concepts. Using digital elevation model (DEM), the topographic index (or wetness index, WI, i.e., $\ln(a/\tan\beta)$, where a is specific catchment area and $\tan\beta$ is local slope) can be computed for each high-resolution pixel of a model grid cell. A lowland pixel corresponds to a greater WI. $F_{\max}$ is the sum of fractional area of subgrid pixels with WI being equal to or larger than the grid cell mean WI (consult *Niu et al.* [2005] for details). We used a global mean $F_{\max}$ derived from HYDRO1K 1 km WI data, i.e., 0.38, in this study. F_{frz} is a fractional impermeable area as a function of soil ice content of the surface soil layer [*Niu and Yang*, 2006]. The runoff decay factor, f = 6.0 globally, is calibrated against global runoff data through sensitivity experiments.

[26] The groundwater discharge (base flow or subsurface runoff) rate is parameterized as:

$$R_{sb} = R_{sb,\max}e^{-\Lambda - f\left(z_{\nabla} - z'_{bot}\right)} \quad (9)$$

where $R_{sb,\max}$ (= 5.0×10^{-4}mm/s globally) was calibrated against global runoff data through sensitivity tests [*Niu et al.*, 2007]. Λ is the grid cell mean WI. We used its global mean value, Λ = 10.46, derived from HYDRO1K 1 km WI data. Because the interactions between groundwater discharge and the water table depth, a greater Λ would ultimately increase groundwater level and thus soil moisture. The accuracy of WI strongly depends on the resolution of digital elevation model (DEM) [*Wolock and McCabe*, 2000]. Usually, WI derived from a higher resolution DEM, e.g., 2 m, is much smaller than that from a coarse resolution, e.g., 1 km, due mainly to the more accurate, greater slope of the higher resolution DEM. To compensate for the error induced by the unrealistically large Λ derived from the HYDRO1K 1 km WI data, we introduced an extra term z'_{bot} = 2 m, the depth of the model bottom. For a specific application, we strongly suggest to derive Λ from high-resolution (meters) DEM if available.

3.5. Leaf Dynamics

[27] The dynamic leaf model [*Dickinson et al.*, 1998] describes carbon budgets for various parts of vegetation (leaf, wood, and root) and soil carbon pools (fast and slow). We added a stem carbon balance equation for simulating stem-rich plants (e. g., corn) [*Yang and Niu*, 2003]. The model accounts for processes including carbon assimilation through photosynthesis, allocation of the assimilated carbon to various carbon pools (leaf, stem, wood, root, and soil), and respiration from each of the carbon pools. The leaf carbon mass, C_{leaf}, (g m^{-2}) is computed from:

$$\frac{\partial C_{leaf}}{\partial t} = F_{leaf}A - \left(S_{cd} + T_{leaf} + R_{leaf}\right)C_{leaf} \quad (10)$$

where A is the total carbon assimilation rate of the sunlit and shaded leaves (g m^{-2} s^{-1}) (see Appendix B). F_{leaf} is the fraction of the assimilated carbon allocated to leaf and parameterized as a function of LAI; $F_{leaf} = e^{(0.01*LAI(1-\exp(\chi LAI))}$, where χ is a vegetation-type-dependent parameter [*Gulden et al.*, 2007]. In early growing season, when LAI is small, this formulation results in a greater allocation of the assimilated carbon to leaf than that used by *Dickinson et al.* [1998]. S_{cd} is the death rate due to cold and drought stresses, and T_{leaf} is the rate of leaf turnover due to senescence, herbivory, or mechanical loss [see *Dickinson et al.*, 1998]. R_{leaf} is the leaf respiration rate including maintenance and growth respiration [*Bonan*, 1996]. LAI is converted from C_{leaf} using specific leaf area (m^2 g^{-1}), a vegetation-type-dependent

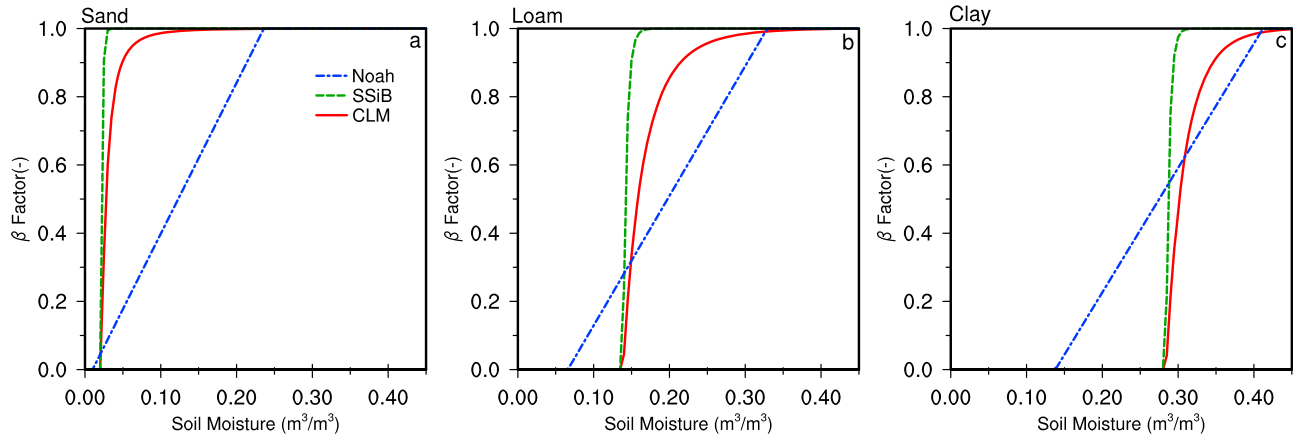

Figure 3. Various soil moisture factors controlling stomatal resistance (β factors) varying with soil moisture for (a) sand, (b) loam, and (c) clay.

parameter vegetation greenness fraction (GVF). GVF is then simply converted from LAI:

$$F_{veg} = 1 - e^{-0.52LAI}. \tag{11}$$

4. Options of Schemes for Various Physical Processes

4.1. Dynamic Vegetation

[28] We designed two options for dynamic vegetation: (1) off and (2) on. When it is turned on, LAI and GVF are predicted from the dynamic leaf model as described in section 3.5, and the option for stomatal resistance must be Ball-Berry type. When the switch is turned off, monthly LAI is prescribed for various vegetation types, GVF comes from a monthly GVF climatological values, and the option for stomatal resistance can be either Ball-Berry type or Jarvis type.

4.2. Stomatal Resistance

[29] We designed two options for stomatal resistance: (1) Ball-Berry type [*Ball et al.*, 1987; *Collatz et al.*, 1991, 1992; *Sellers et al.*, 1996; *Bonan*, 1996] and (2) Jarvis type [*Jarvis*, 1976]. The Ball-Berry-type stomatal resistance for sunlit and shaded leaves is related to their photosynthesis rates, which are controlled by the sunlit and shaded PAR, respectively (see Appendix B). *Chen et al.* [1996] described the Jarvis-type stomatal resistance scheme in detail. We modified the scheme to accommodate sunlit and shaded LAI and their associated PAR.

4.3. Soil Moisture Factor Controlling Stomatal Resistance, β Factor

[30] We implemented three options for this factor: (1) Noah type using soil moisture, (2) CLM type using matric potential, and (3) SSiB type also using matric potential but expressed by a different function [*Xue et al.*, 1991]. The Noah-type factor is parameterized as a function of soil moisture:

$$\beta = \sum_{i=1}^{N_{root}} \frac{\Delta z_i}{z_{root}} \min\left(1.0, \frac{\theta_{liq,i} - \theta_{wilt}}{\theta_{ref} - \theta_{wilt}}\right) \tag{12}$$

where θ_{wilt} and θ_{ref} are soil moisture at witling point (m^{-3} m^{-3}) and a reference soil moisture (m^{-3} m^{-3}) (close to field capacity), respectively. Both depend on soil type. N_{root} and z_{root} are total number of soil layers containing roots and total depth of root zone, respectively. The CLM-type factor [*Oleson et al.*, 2004] is a refined version of that of BATS [*Yang and Dickinson*, 1996]:

$$\beta = \sum_{i=1}^{N_{root}} \frac{\Delta z_i}{z_{root}} \min\left(1.0, \frac{\psi_{wilt} - \psi_i}{\psi_{wilt} - \psi_{sat}}\right) \tag{13}$$

where $\psi_i = \psi_{sat}\,(\theta_{liq,i}/\theta_{sat})^{-b}$ is the matric potential of the ith layer soil, ψ_{sat} is the saturated matric potential, and ψ_{wilt} is the wilting matric potential, which is −150 m independent of vegetation and soil types. The SSiB-type β factor is:

$$\beta = \sum_{i=1}^{N_{root}} \frac{\Delta z_i}{z_{root}} \min\left(1.0, 1.0 - e^{-c_2 \ln(\psi_{wilt}/\psi_i)}\right) \tag{14}$$

where c_2 is a slope factor ranging from 4.36 for crops to 6.37 for broadleaf shrubs [see *Xue et al.*, 1991, Table 2]. The CLM-type β factor shows a sharper and narrower range of variation with soil moisture than the Noah type does (Figure 3). The SSiB β factor (c_2 = 5.8 in Figure 3) is even steeper than the CLM type. These three options represent a great uncertainty in formulating the β factor in LSMs.

4.4. Runoff and Groundwater

[31] We designed four options for runoff and groundwater schemes. Option 1 is the TOPMODEL-based runoff scheme with the simple groundwater (hereafter SIMGM) [*Niu et al.*, 2007]. Option 2 is a simple TOPMODEL-based runoff scheme with an equilibrium water table [*Niu et al.*, 2005] (hereafter SIMTOP). Similar to SIMGM, SIMTOP parameterizes both surface and subsurface runoff as functions of the water table depth but with a sealed bottom of the soil column (zero-flux lower boundary condition) in accordance with one of the TOPMODEL assumptions, i.e., the exponential decay of saturated hydraulic conductivity. Option 3 is an infiltration-excess-based surface runoff scheme with a gravitational free-drainage subsurface runoff scheme as used in the original Noah [*Schaake et al.*, 1996]. Option 4 is

the BATS runoff scheme, which parameterized surface runoff as a 4th power function of the top 2 m soil wetness (degree of saturation) and subsurface runoff as gravitational free drainage [*Yang and Dickinson*, 1996].

4.5. Surface Exchange Coefficient for Heat, C_H

[32] Two options are implemented. Option 1 is the one used in Noah version 3.0 (hereinafter Noah V3) [*Chen et al.*, 1997] (hereinafter Chen97):

$$C_H = \frac{\kappa^2}{\left[\ln\left(\frac{z}{z_{0m}}\right) - \psi_m\left(\frac{z}{L}\right) + \psi_m\left(\frac{z_{0m}}{L}\right)\right]\left[\ln\left(\frac{z}{z_{0h}}\right) - \psi_h\left(\frac{z}{L}\right) + \psi_h\left(\frac{z_{0h}}{L}\right)\right]} \quad (15)$$

where κ is the von Kármán constant, L is the Monin-Obukhov length, and z is the reference height. z_{0h} and z_{0m} are roughness lengths for heat and momentum, respectively, and $z_{0h} = z_{0m}\exp(-\kappa C\sqrt{\mathrm{Re}^*})$, where Re* is the roughness Reynolds number, and C = 0.1. Option 2 is based on more general Monin-Obukhov similarity theory [*Brutsaert*, 1982], hereinafter, M-O:

$$C_H = \frac{\kappa^2}{\left[\ln\left(\frac{z-d_0}{z_{0m}}\right) - \psi_m\left(\frac{z-d_0}{L}\right)\right]\left[\ln\left(\frac{z-d_0}{z_{0h}}\right) - \psi_h\left(\frac{z-d_0}{L}\right)\right]} \quad (16)$$

where d_0 is the zero-displacement height, and $z_{0h} = z_{0m}$. Both options take the same stability correction functions (ψ_m and ψ_h) for stable and unstable conditions as described in detail by Chen97. Option 1 accounts for the difference between z_{0h} and z_{0m} but does not account for d_0.

4.6. Supercooled Liquid Water in Frozen Soil

[33] When soil freezes, water close to soil particles remains in liquid form due to capillary forces exerted by fine soil particles. For such a reason, only the excessive liquid water beyond $\theta_{liq\max,i}$ (the upper limit of the supercooled liquid water) can be frozen, and the amount of liquid water for the ith soil layer is either $\theta_{liq\max,i}$ or $\theta_{liq,i}$, whichever is less. $\theta_{liq\max,i}$ is a function of soil temperature and texture (clay content) and can be derived from various forms of freezing-point depression equation.

[34] Two options are implemented. Option 1 takes a more general form of the freezing-point depression equation [*Niu and Yang*, 2006] (hereinafter NY06), while option 2 takes a variant of the freezing-point depression equation [*Koren et al.*, 1999] (hereinafter Koren99) with an extra term, $(1 + 8\theta_{ice})^2$. This extra term accounts for the increased interface between soil particles and liquid water due to the increase of ice crystals. Option 2 needs to be solved iteratively and generally produces more liquid water than Option 1 because of the extra term.

4.7. Frozen Soil Permeability

[35] Two options are implemented. Option 1 adopts a scheme proposed by NY06, which assumes that a model grid cell consists of permeable and impermeable areas and thus uses the total soil moisture to compute hydraulic properties of the soil. Option 2 inherits the Koren99 scheme in Noah V3, which uses only the liquid water volume to compute hydraulic properties. Option 1, which assumes that soil ice has a linear (smaller) effect on infiltration, generally produces more permeable frozen soil than option 2 does, which assumes soil ice has a nonlinear (greater) effect on soil permeability.

4.8. Radiation Transfer

[36] Three options are designed for radiation transfer through the vegetation canopy with regard to subgrid distributions of vegetation. Option 1 is the modified two-stream scheme briefly described in section 2.2.1. Further details can be given by *Yang and Friedl* [2003] or *Niu and Yang* [2004]. Option 1 assumes that the gap probability is a function of SZA and the 3-D structure of the vegetation canopy with a maximum between-canopy gap of 1.0–GVF (when the sun is overhead). Option 2 applies the two-stream approximation to the entire grid cell, and thus the between-canopy gap probability is zero. Option 3 applies the two-stream approximation only to the vegetated fraction and the between-canopy gap probability equals to 1.0–GVF. Option 3 is equivalent to a "mosaic" model, usually exposing too much understory vegetation or snow to solar radiation.

4.9. Snow Surface Albedo

[37] We implemented two options for snow surface albedo: one adopted from BATS [see *Yang et al.*, 1997] and the other from CLASS [*Verseghy*, 1991]. The BATS scheme computes snow surface albedo for direct and diffuse radiation over visible and near-infrared wave bands [*Dickinson et al.*, 1993], accounting for fresh snow albedo, variations in snow age, SZA, grain size growth, and impurity (dirt or soot on snow). The CLASS scheme simply computes the overall snow surface albedo accounting for fresh snow albedo and snow age and performs well in simulating snow age and surface albedo. The BATS scheme usually produces larger snow surface albedo than the CLASS scheme does due to its weaker aging effects.

4.10. Partitioning Precipitation Into Rainfall and Snowfall

[38] Partitioning precipitation into rainfall and snowfall in most LSMs uses surface air temperature, T_{air}, as a criterion. We implemented three options: (1) the relatively complex functional form of *Jordan* [1991], (2) the BATS scheme, which assumes all precipitation as snowfall when $T_{air} < T_{frz} + 2.2$ K and rainfall otherwise, and (3) simply assuming all precipitation as snowfall when $T_{air} < T_{frz}$ and rainfall otherwise. In midlatitude and coastal regions where T_{air} frequently varies around the freezing point, the modeled snow accumulation is very sensitive to these choices.

5. Model Assessments at Local Scales

5.1. Surface Fluxes

[39] To test the augmented Noah LSM's performance in simulating the surface energy and water fluxes, we selected the widely used, high-quality atmospheric forcing and flux measurements averaged over stations within the First ISLSCP (International Satellite Land Surface Climatology Project) Field Experiment (FIFE) 15 km × 15 km domain [*Betts and Ball*, 1998]. We used the 1987 data set. The surface atmospheric forcing data are averaged over 10 Portable Automatic Meteorological (PAM) stations, while the surface flux measurements were averaged over 22 sites.

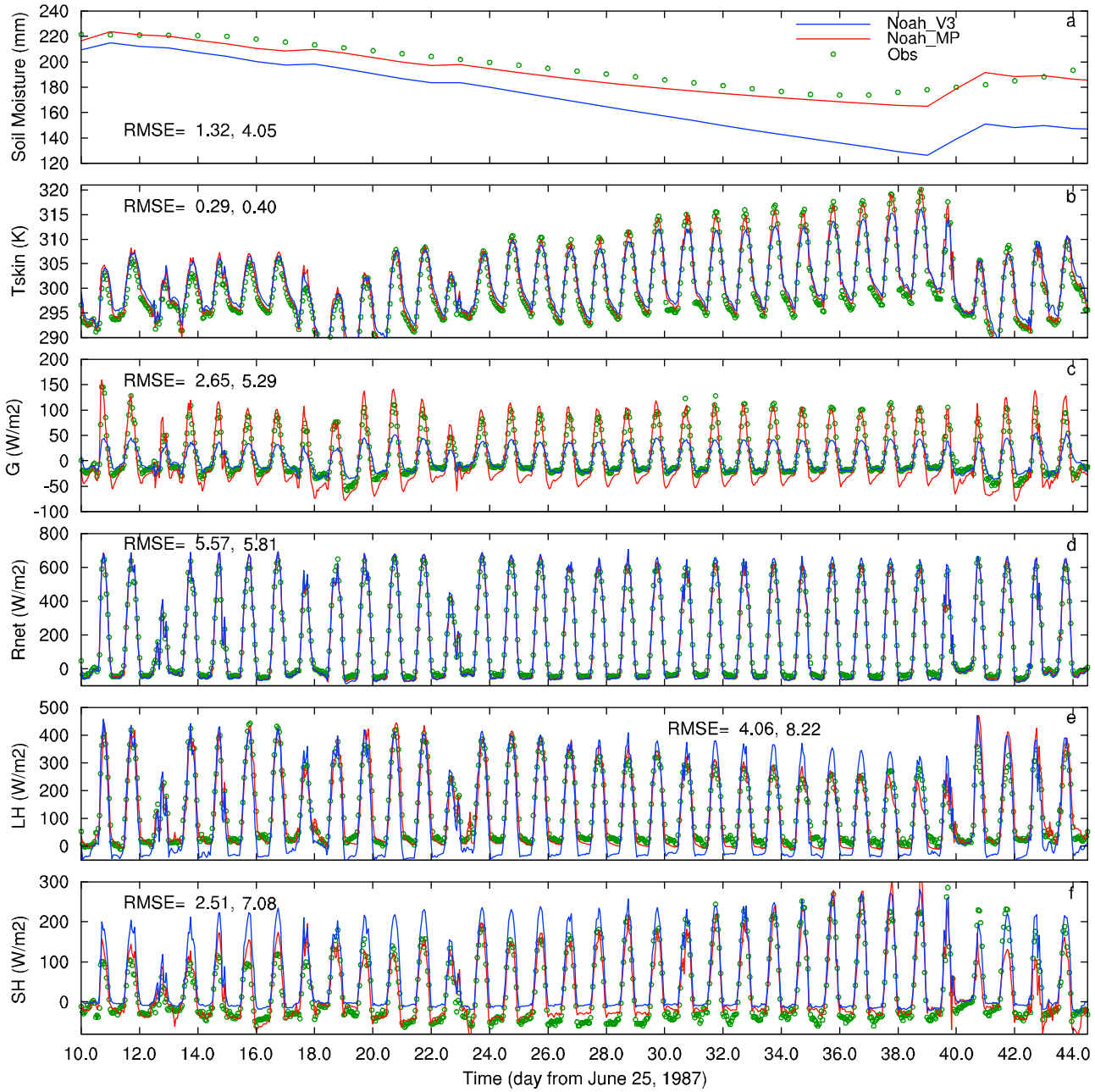

Figure 4. Model simulated versus FIFE observations, (a) top 1 m soil moisture, (b) skin temperature, (c) ground heat flux, (d) net radiation, (e) latent heat, and (f) sensible heat fluxes. Root-mean-square errors (RMSEs) in sequence for Noah-MP and Noah V3 are also shown in each panel for each variable.

The FIFE domain is predominately grassland of moderate topography.

[40] We ran both Noah V3 and Noah-MP for two months starting from 25 June 1987. Soil moisture for both models was initialized using the gravimetric measurements (20-site average) for the top 10 cm layer while using neutron probe measurements (31-site average) for the rest layers. We choose the model physics options for Noah-MP as follows: Jarvis-type canopy stomatal resistance and Noah β factor for stomatal resistance, which are the same as in Noah V3, SIMGM for runoff and groundwater and M-O scheme for the surface exchange coefficient, which are different from Noah V3. The combination of the options is equivalent to EXP4 of paper 2 [*Yang et al.*, 2011]. We did not turn on the dynamic vegetation for this short-period simulation, because the model needs at least a year-long data set for spinning up to determine the initial leaf mass. All the model parameters are the same as those optimized in the global simulations in the companion paper, except that the roughness length and LAI are calibrated to 0.08 m and 3.0 m^2/m^2 from their globally optimized values, which are 0.06 m and 2.0 m^2/m^2, respectively.

[41] We focus on a dry-down period when analyzing the modeling results as shown in Figure 4. Both Noah-MP and Noah V3 simulate well net radiation (Figure 4d). However, Noah-MP produces a smaller root mean square error

(RMSE) for net radiation than did Noah V3, because Noah-MP produces more accurate outgoing longwave radiation as indicated from a better simulation of surface radiative (or skin) temperature (Figure 4b). Overall, Noah V3 simulated skin temperature well, but about 5 K lower than observations at midday hours during the dry-down period from day 28 to day 39. Noah-MP produces a greater diurnal amplitude for the ground heat flux than did Noah V3 because they use different parameterization schemes for surface soil thermal conductivity. Noah-MP adopts the soil thermal conductivity scheme [*Peters-Lidard et al.*, 1998] of Noah V3 but removes the exponential decay of the surface soil thermal diffusivity with vegetation cover fraction because of the model structural change, i.e., separating the vegetation canopy from the soil surface. Noah-MP simulates the ground heat flux and other variables better than did Noah V3 as indicated from the RMSEs shown in Figure 4, but the better simulations may not hold for all combinations of uncertain parameters. Evaluation of models' performance over the full spectrum of parameter space [*Gulden et al.*, 2008] should be conducted in future model evaluations.

5.2. Snow

[42] To test the model's ability to simulate snow processes, we first tested the model against the Sleeper River data set and then Col de Porte data set because these data sets provide detailed measurements of snow depth, SWE, snow surface albedo, and snow skin temperature. The Sleepers River data set is the observational data set obtained in subcatchment W-3 (8.4 km^2) (44.43°N, 72.42°W) of the Sleepers River watershed (111 km^2), located in the highlands of Vermont, USA. The data set provides atmospheric forcing, snow properties, and streamflow data obtained between 1969 and 1974 at hourly intervals. The W-3 topography is characterized by rolling hills, and the soils are dominated by silty loams. The local vegetation is approximately one third grassland, one third coniferous forest, and one third deciduous forest. Additional details about the Sleepers River watershed data set were provided by *Lynch-Stieglitz* [1994] and *Stieglitz et al.* [1997].

[43] The Col de Porte data set provides measurements of atmospheric forcing and snow properties at hourly intervals at the Col de Porte (45°N, 6°E, 1320 m) in the French Alps [*Brun et al.*, 1992]. This site is characterized by a continuous snow cover from late fall to late spring, with loamy soil and short-grass vegetation. The atmospheric forcing data include air temperature, specific humidity, wind speed, precipitation, downward solar radiation, surface pressure, and downward longwave radiation. The Col de Porte data set also provides a snow/rain index to indicate the snowfall rate.

[44] The model options for Noah-MP in the case of Sleepers River are the same as those for a global application, EXP6, by *Yang et al.* [2011] except that snowfall criterion is changed from option 1 to option 3, i.e., assuming all precipitation as snowfall when $T_{air} < T_{frz}$ and rainfall otherwise. This change is made to be consistent with an earlier study by *Lynch-Stieglitz* [1994]. Correspondingly, Noah V3 uses the same snowfall criterion. The model options for the Col de Porte case are the same as those for the global application EXP6 by *Yang et al.* [2011]. Initial conditions for snow depth and SWE are zero for both the Sleepers River case and the Col de Porte case. Other key parameters are also the same as those optimized in the global simulations of paper 2, e.g., the snow surface roughness length is 0.002 mm, the liquid water holding capacity is 0.03 m^3/m^3, and the melting curve parameter to determine the slope of snow cover fraction [*Niu and Yang*, 2007] is 1.0. Note that, at the Col de Porte, the snowfall rate is provided according to the observed snow/rain criterion.

[45] Similar to other investigations [*Ek et al.*, 2003; *Pan et al.*, 2003; *Mitchell et al.*, 2004; *Livneh et al.*, 2010], Noah V3 produces lower snow surface albedo, less SWE, and a shallower snowpack (Figure 5). Noah-MP captures surface albedo peaks and recessions by using the CLASS scheme which accounts for fresh snow albedo and snow aging processes (Figure 5a). Noah-MP greatly improves the simulation of SWE, snow depth, and snow density (Figures 5b–5d). Consistent with *Livneh et al.* [2010], our sensitivity tests reveal that considering retention of meltwater at midday hours and refreezing of the liquid water at nighttime contributes to the improved simulation in melting season (see section 6.3).

[46] Testing against the Col de Porte detailed measurements of snow properties (Figure 6) and snow skin temperature (Figure 7) reveals that accurate simulations of the diurnal cycle of snow skin temperature are of significant importance to ensure accurate simulations of snowmelt and refreezing of liquid water and hence improvements of snow simulations. The observed snow skin temperature shows obvious diurnal variations, i.e., at melting/freezing point during midday hours because of the coexistence of ice and meltwater and subzero temperatures at night when the meltwater is refreezing. Noah V3 simulates higher temperatures at night (lower cold content) and longer duration of melting during the day and even at night, for instance, from day 42 to day 54. However, Noah-MP greatly improves the simulation of snow skin temperature for most of the snow season, ensuring a more realistic simulation of timing and duration of the snowpack melting.

5.3. Runoff

[47] Figure 8 shows the testing results using the data set in the W-3 subcatchment of the Sleepers River watershed. Noah V3 produces too many peaks, higher peak values, and lower values in recession periods due mainly to the low soil permeability for frozen soil. Noah V3 considers supercooled liquid water for subzero soil temperatures using the freezing-point depression equation [*Koren et al.*, 1999]. Noah V3 computes hydraulic conductivity as a function of soil liquid water content and accounts for the effects of fractional frozen area on surface runoff but not for soil permeability. Noah-MP introduces the effects of fractional frozen area on soil permeability and separates a model grid cell into permeable and impermeable fractions following *Niu and Yang* [2006] and thus enhances the grid cell permeability, allowing more water to infiltrate through soil layers. In addition, a better simulation of snowmelt by Noah-MP also contributes to the better simulation of runoff. Note that Noah-MP introduces the TOPMODEL concepts to improve the partitioning of surface runoff and subsurface runoff [*Niu et al.*, 2005]. The TOPMODEL concepts link runoff (both surface runoff and base flow) to the water table depth (or water storage) through exponential functions [*Niu et al.*, 2005].

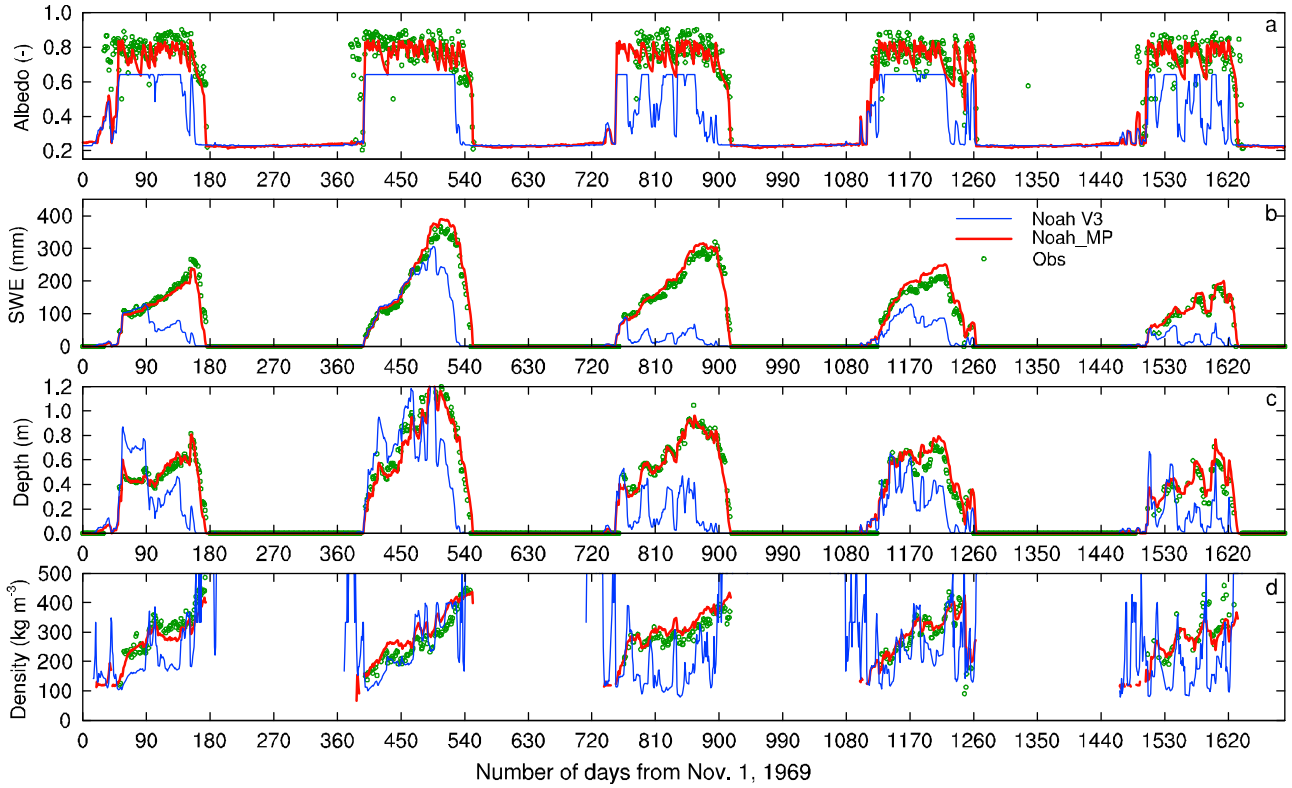

Figure 5. Model simulated versus observations over W3 catchment of the Sleepers River: (a) snow surface albedo, (b) SWE, (c) snow depth, and (d) snow density.

However, it may fail in arid or semiarid regions where the water table depth is too deep and infiltration-excess runoff is dominant (G.-Y. Niu et al., The role of water subsidy on vegetation dynamics in a semiarid grassland catchment: Comparison between field measurements and 3-D ecohydrological modeling, submitted to *Water Resources Research*, 2011).

6. Role of Optional Schemes in Interpreting Modeling Results

[48] In this section, we demonstrate that, Noah-MP is an effective research tool through which differences in modeling results can be explained by sensitivity experiments using different options of parameterization schemes for a specific process in the same model framework.

6.1. Surface Exchange Coefficients

[49] Noah V3 usually produces a cold bias in surface skin temperature in the arid western U.S. during the midday hours [*Yang et al.*, 2011]. This cold bias may possibly be caused by improper representations of the processes controlling surface energy fluxes or related hydrological processes. Without multiple options, it is difficult to pinpoint the exact causes in the context of the complex coupling system of atmospheric, hydrological, and ecological processes. We conducted an additional experiment by simply replacing the M-O scheme for the surface exchange coefficient with the original scheme in Noah V3, i.e., Chen97 (equation (15)) using the FIFE data set.

[50] Noah-MP with the Chen97 scheme produced a greater C_H than Noah-MP with the M-O scheme but less than Noah V3 (Figure 9). Although Noah-MP differs from Noah V3 in many other aspects, only changing the C_H

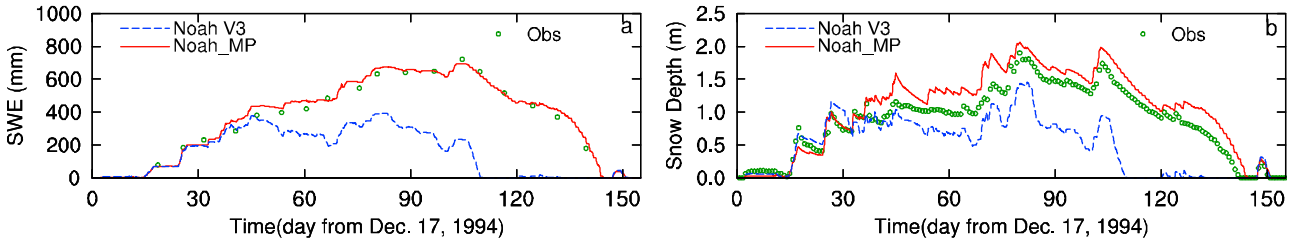

Figure 6. Model simulated versus observed at Col de Porte, France: (a) SWE and (b) snow depth.

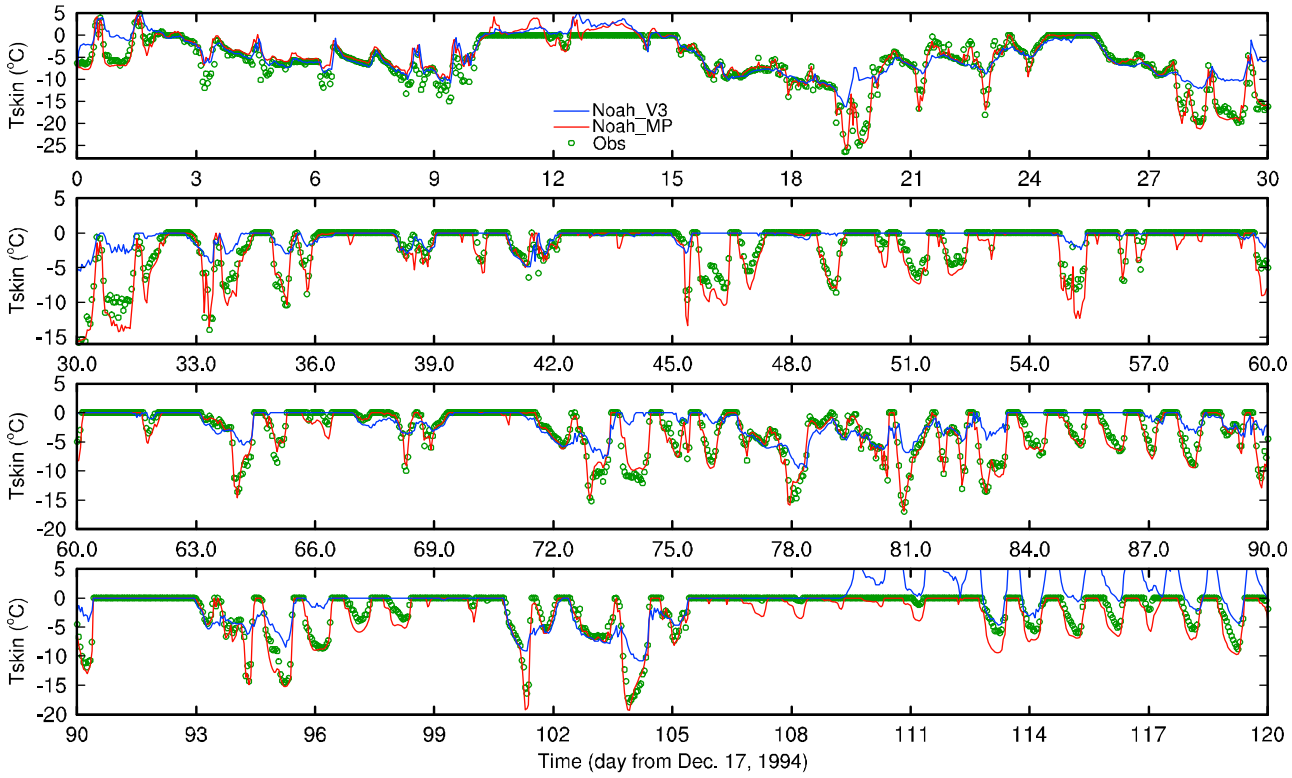

Figure 7. Model simulated skin temperature in comparison with observed at Col de Porte, France.

scheme back to that used in Noah V3 (i.e., Chen97) almost reproduced the skin temperature modeled by Noah V3, both showing significant cold biases during the midday hours during the dry-down period. A greater C_H means more efficient ventilation and greater cooling of the land surface during the summer daytime. This reflects the important role of C_H in controlling the surface skin temperature. Noah-MP with these optional C_H schemes can readily determine the major cause for the cold biases. *Yang et al.* [2011] discussed how the optional M-O scheme corrects the cold biases over the arid western U.S., while not affecting the simulation over the eastern U.S.

6.2. Drought Stress Factors

[51] The soil moisture factor controlling the stomatal resistance, or the drought stress factor (the β factor) is critical for terrestrial ecosystem dynamics and its interactions with climatic and hydrologic processes. We conducted

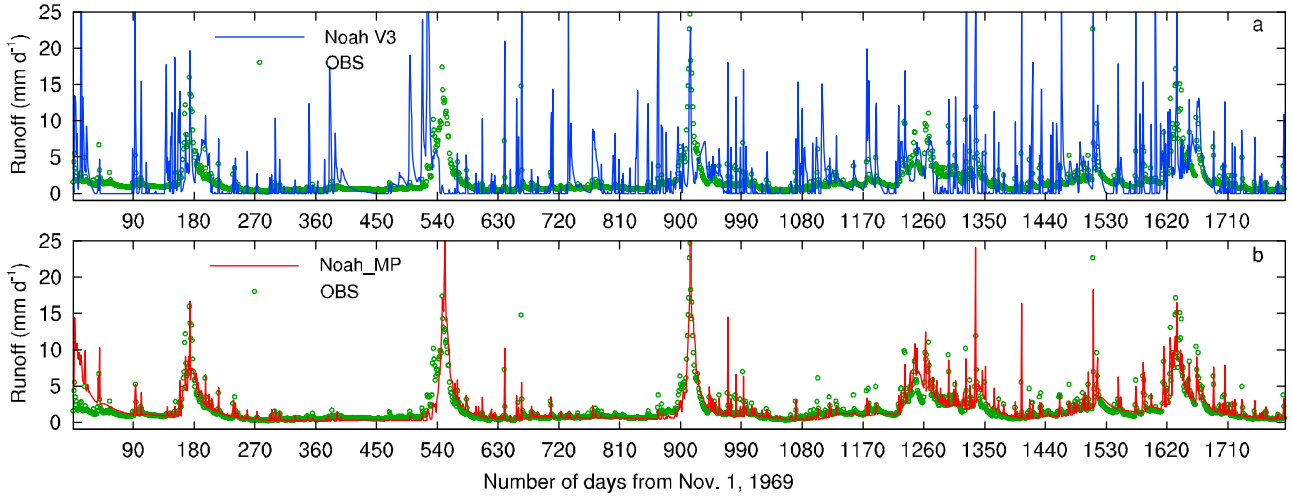

Figure 8. (a) Noah V3 and (b) Noah-MP simulated daily runoff in comparison with streamflow observations in W-3 subcatchment of the Sleepers River watershed, Vermont.

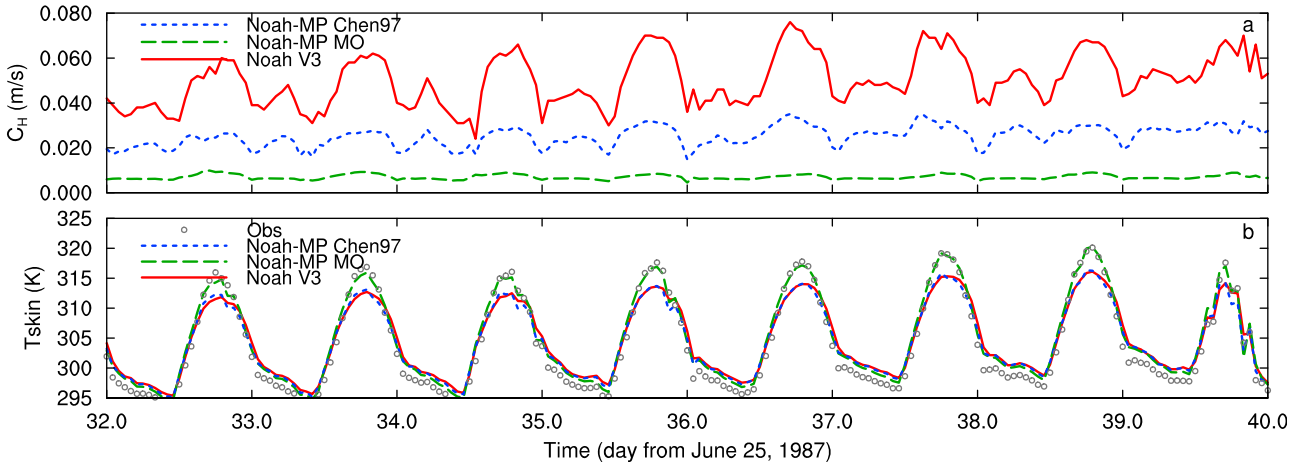

Figure 9. Modeled (a) surface exchange coefficient for heat and (b) skin temperature by Noah-MP with different schemes of surface exchange coefficient (Chen97 scheme and M-O scheme) and Noah V3.

experiments to investigate the effects of the factor on the surface energy fluxes. We ran Noah-MP with different β factors, i.e., the Noah-type (equation (12)) and CLM-type (equation (13) β factors using the FIFE data set. During the dry-down period from day 23 to day 39, Noah-MP with the CLM β factor produces a faster decay of the midday latent heat flux, and for such a reason, it consumes less soil water, resulting in smaller soil moisture variability than did the Noah β factor (Figure 10). We are not intended to conclude that the CLM β factor performs worse than the Noah β factor, because adjusting model parameters or changing schemes for other processes may also correct this mismatch. However, through the multiple optional schemes for the β factor within the same model framework, the role of different β factors in controlling surface latent fluxes and soil moisture variability can be readily interpreted. This can also help explain why CLM version 3.5 produced smaller seasonal variability in soil moisture [*Oleson et al.*, 2004].

6.3. Why Does Noah-MP Improve Snow Simulations?

[52] The improvements in snow simulations by Noah-MP may be attributed to changes in the model structure (i.e., the separation of the vegetation canopy from snow surface), model layers (3 snow layers in Noah-MP versus a bulk layer in Noah V3), computational methods for snow skin temperature (the iterative surface energy balance method in

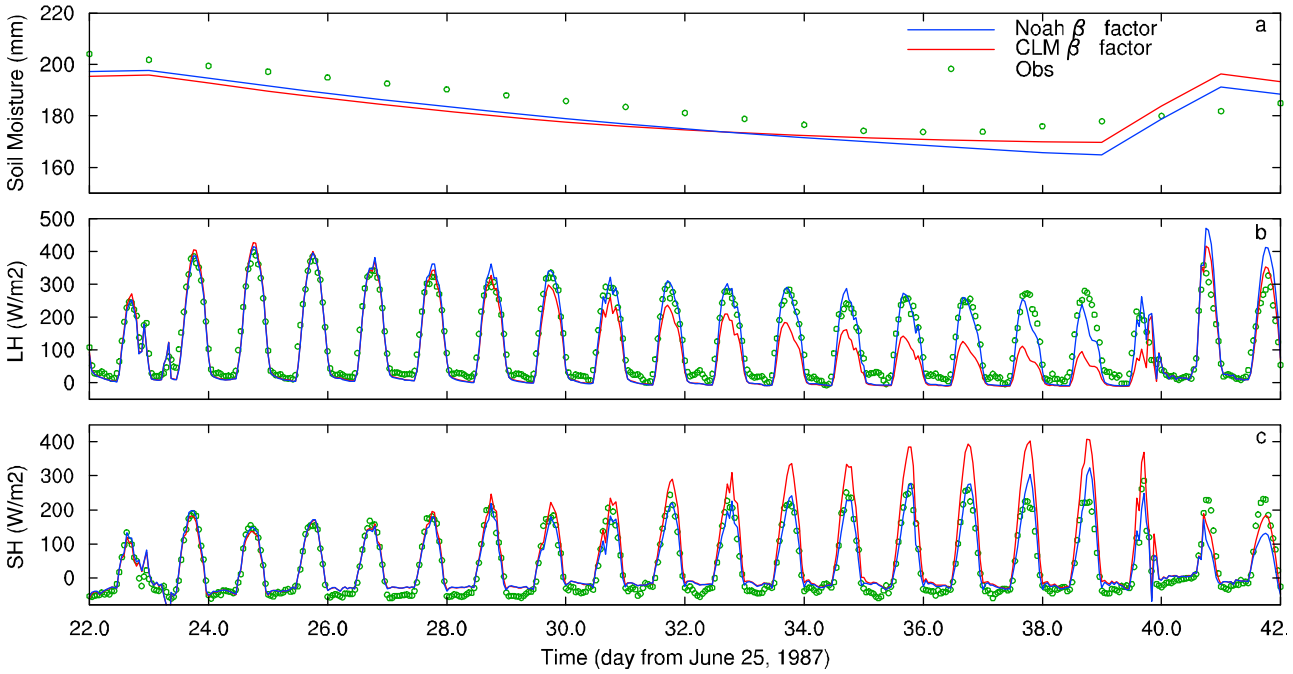

Figure 10. Noah-MP simulated (a) top 1 m soil moisture, (b) latent heat, and (c) sensible heat fluxes using Noah β and CLM β factors.

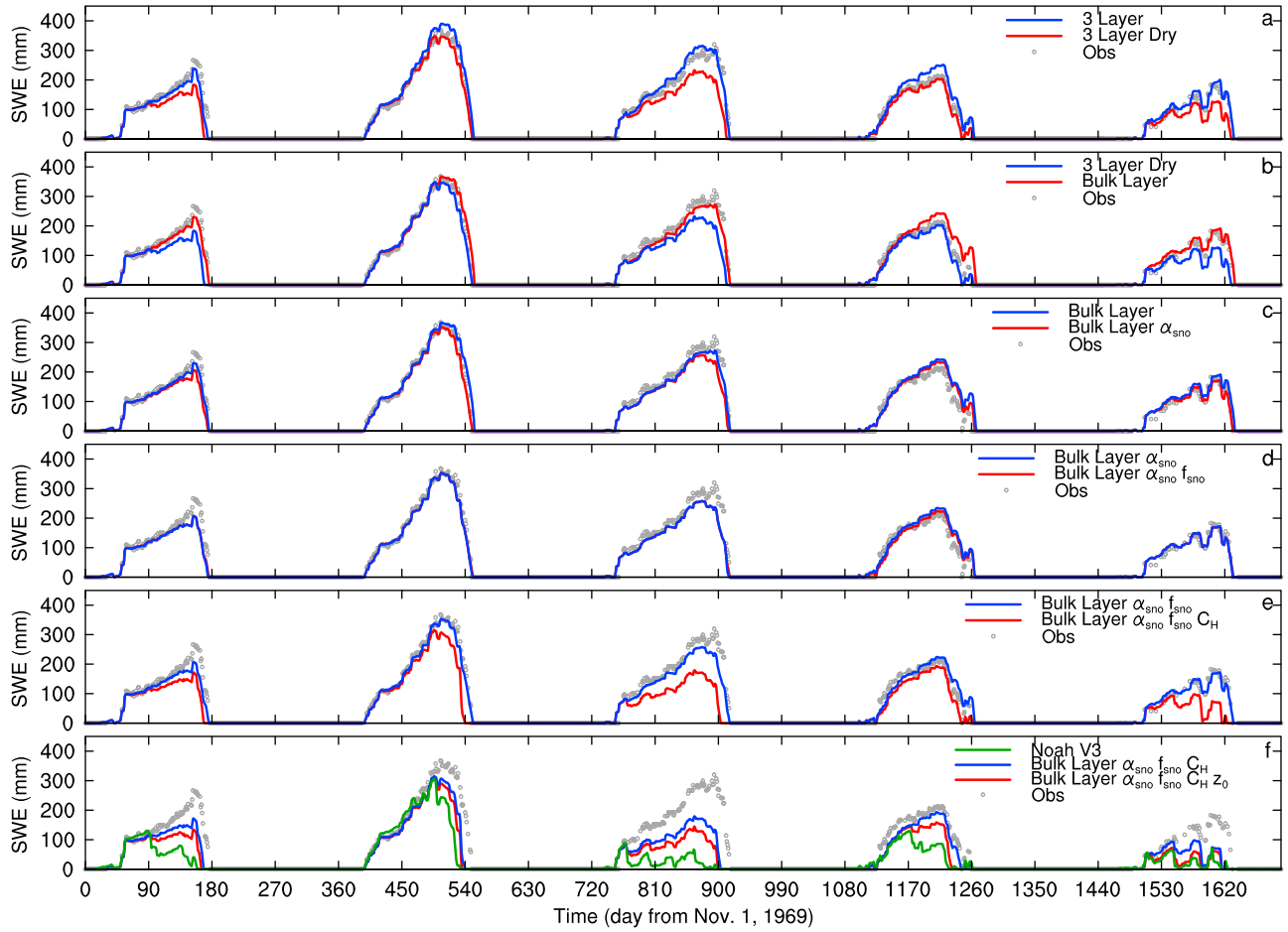

Figure 11. SWE modeled by evolutional versions of Noah-MP (see text for the meanings of the legends in each panel) in comparison with those of observed and modeled by Noah V3 (Figure 11f only).

Noah-MP versus the noniterative surface energy balance method in Noah V3), and parameterization schemes for other processes (e.g., snow surface albedo, snow cover fraction, surface turbulent exchange coefficient, liquid water retention and refreezing, snow surface roughness length, etc.). Because the land surfaces in both the Sleepers River and Col de Porte are short grasses, being readily buried by the snowpack for most of the modeling period, the effects of separating the canopy from snow surface on snow simulation is insignificant and can be excluded. Noah-MP retains most of the schemes of Noah V3 except for the snowmelt scheme and the scheme to compute the skin temperature. Therefore, we conducted experiments through using a series of evolutional versions that gradually reverts Noah-MP back to Noah V3 to see which of these evolutional Noah-MP versions can reproduce the results from Noah V3, thereby shedding light on the role of a particular physical process in the snow simulations.

[53] Using the Noah-MP three-layer structure, we first removed the liquid water retention by assuming the liquid water holding capacity to zero ($\theta_{liq,\max,i}$ = 0.0 m^3/m^3). Without liquid water retention and refreezing at night (i.e., "3 Layer Dry" as represented in the legend of Figure 11), Noah-MP produces less SWE and shorter snow seasons (Figure 11a). We then changed the three-layer snow of Noah-MP to a bulk, combined layer of the snowpack and the uppermost soil layer, the same as Noah V3 ("Bulk Layer"). In such a case, because of no overlying snow layers, the scheme for compaction due to weight is then a self-compaction scheme [*Sun et al.*, 1999], i.e., the snowpack is compacted by half of its total weight. This scheme is demonstrated efficient to produce decent results of snow density (not shown). This "bulk layer" version does not account for liquid water within the snowpack. It predicts more snow mass and longer snow seasons (Figure 11b), likely because of the greater thermal inertia of the bulk, combined soil and snow layer. The "bulk layer" version still uses the same melting scheme, i.e., equation (5) to compute melting energy, except that T_i^{N+1} for snow layers is replaced by T_1, the temperature of the bulk layer. The heat capacity of the bulk layer is much greater than that of a thin snow layer, producing a spuriously greater thermal inertia for solving T_1. Based on the "Bulk Layer," the snow surface albedo (α_{sno}) scheme in Noah-MP is then changed from the CALSS type (see section 4.9) to the one of Noah V3 (0.64 prescribed for grassland), i.e., the experiment "Bulk Layer α_{sno}." The Noah V3 α_{sno} scheme produced slightly less SWE (Figure 11c) during the melting seasons due to its smaller α_{sno} (not shown, but readers can refer to Figure 5a).

[54] We then change the snow cover fraction (f_{sno}) scheme from *Niu and Yang* [2007] to that of Noah V3 (which in *Ek et al.*'s [2003] work rapidly increases to 1.0 when SWE is changing from 0 to 40 mm for grassland), i.e., the experiment "Bulk Layer α_{sno} f_{sno}." Because the Noah V3 f_{sno} scheme produced f_{sno} very close to that with *Niu and Yang*'s [2007] scheme, this change does not have a noticeable effect (Figure 11d). Based on the above changes, the C_H scheme is then changed from the M-O scheme to Chen97 scheme ("Bulk Layer α_{sno} f_{sno} C_H"). Chen97 produces less snow and shorter snow seasons (Figure 11e), because it usually produces a greater C_H or more efficient exchanges of sensible heat with the atmosphere (negative in springtime) and a greater sublimation. We finally changed the snow surface roughness length (z_0) from 0.002 m to 0.1 m (the same as in Noah V3) on the basis of all the above changes ("Bulk Layer α_{sno} f_{sno} C_H Z_0"). This change further degrades the simulation. We think 0.1 m z_0 for snow in Noah V3 is not reasonable. We then change z_0 from 0.1 m to 0.002m in Noah V3. However, Noah V3 is insensitive to this change. In addition, most of the sensitivities obtained above through Noah-MP were not obtained through Noah V3 or Noah V3 is less sensitive to these changes than does Noah-MP. This is most likely because of the different schemes for computing the snow skin temperature and snowmelt energy as used in Noah-MP and Noah V3.

7. Summary

[55] Through community efforts, we have augmented the widely used community Noah LSM as follows.

[56] 1. We added a separated vegetation canopy layer into the baseline Noah LSM to better represent the vegetation effects on the surface energy, water, and carbon budgets. In addition, this separate canopy layer facilitates the coupling with a dynamic vegetation model, which requires PAR, photosynthesis, and leaf temperature of sunlit and shaded leaves.

[57] 2. We developed a "semitile" subgrid scheme to account for the effects of vegetation canopy gaps varying with SZA and the 3-D canopy structure on radiation transfer. The semitile scheme computes shortwave radiation transfer over the entire grid cell but computes latent heat, sensible heat, and ground heat fluxes separately over vegetation-covered and vegetation-free areas.

[58] 3. We added a three-layer snow model and a snow interception model into the Noah model. The three-layer model represents percolation, retention, and refreezing of meltwater within the snowpack. The snow interception model accounts for a greater interception capacity for snowfall than rainfall and improves the calculation of sublimation and surface albedo.

[59] 4. We introduced a more permeable frozen soil into the Noah LSM by separating a grid cell into permeable and impermeable fractions.

[60] 5. We added a simple groundwater model with a TOPMODEL-based runoff scheme into the Noah model. The simple groundwater model is a revised version of that by *Niu et al.* [2007] to better simulate runoff and soil moisture mean states and their variability.

[61] 6. We added a short-term dynamic model to predict LAI and GVF. LAI and GVF are converted from the predicted leaf carbon mass, which is controlled by carbon allocation of the assimilated carbon through photosynthesis of sunlit and shaded leaves, maintenance and growth respirations, leaf turnover and death due to drought and cold stress.

[62] On the basis of the augmented Noah LSM, we then designed optional schemes for dynamic vegetation, stomatal resistance, the β factor, runoff, radiation transfer, aerodynamic resistance, snow surface albedo, supercooled liquid water in frozen soil, frozen soil permeability, and partitioning precipitation into snowfall and rainfall.

[63] We tested the augmented Noah LSM against FIFE observed surface fluxes. Noah-MP improves the simulation of surface radiative temperature during dry periods over Noah V3. Noah-MP produces greater amplitude of ground heat flux due mainly to removing the exponential decay of the surface soil thermal conductivity with vegetation cover fraction, while it indirectly accounts for the effects of vegetation on the ground heat flux through the exponential decay of solar radiation incident on the ground surface. Noah-MP also shows improvements in simulating sensible heat and latent heat fluxes given the model default parameters over FIFE. However, it is subject to further testing efforts for various combinations of uncertain parameters to obtain a fair comparison as suggested by *Gulden et al.* [2008].

[64] We tested the model's ability to simulate snow depth, SWE, and runoff observations over W3 catchment of the Sleepers River, Vermont, and diurnal snow skin temperature at a French site. Noah-MP shows apparent improvements in reproducing SWE, snow depth and runoff over Noah V3. It improves SWE simulation in both accumulation and melting periods due mainly to the more accurate simulation of the diurnal cycle of snow skin temperature. It also improves the simulation of runoff peaks and recessions by introducing a more permeable frozen soil. Noah-MP enhances the sensitivity of modeled SWE to various processes over Noah V3 most likely because of enhanced conceptual realism introduced in Noah-MP to compute the snow skin temperature and snowmelt energy. The modeling through the evolutional versions of Noah-MP in comparison with the default Noah LSM shows that Noah-MP with multiple optional schemes helps pinpoint the causes for deficiencies in the Noah LSM.

[65] Noah-MP is demonstrated to be a viable research tool through which the role of a specific process in controlling surface temperature and fluxes can be readily investigated by comparing alternative parameterizations within the same model framework. This feature may also be useful for interpreting modeling results from different land surface models and for quantifying uncertainties in different parameterizations.

Appendix A: Formations of Surface Energy Fluxes

[66] The formulations of energy fluxes over fractional areas of bare ground, vegetated ground, and the vegetation canopy are summarized in Table A1.

Appendix B: Ball-Berry-Type Stomatal Resistance and Photosynthesis Rate

[67] The Ball-Berry stomatal resistance per unit LAI of shaded and sunlit leaves, $r_{s,i}$ ($r_{s,shd}$ and $r_{s,sun}$), is related to

Table A1. Formulations of Energy Fluxes Over Different Surfaces[a]

	Bare Ground Fraction, $1 - F_{veg}$	Vegetated Ground Fraction, F_{veg}	Vegetation Canopy, F_{veg}
Longwave radiation	$L_{ag,b} = -\alpha_{gL} L_{air}\downarrow + \varepsilon_g \sigma T_{g,b}{}^4$	$L_{ag,v} = -\alpha_{gL} L_v\downarrow + \varepsilon_g \sigma T_{g,v}{}^4$ where $L_v\downarrow = (1-\alpha_{vL}) L_{air}\downarrow + \varepsilon_v \sigma T_v{}^4$	$L_{av} = -\alpha_{vL}\,(L_{air}\downarrow + L_g\uparrow) + 2\varepsilon_v \sigma T_v{}^4$ where $L_g\uparrow = (1-\alpha_{gL}) L_v\downarrow + \varepsilon_g \sigma T_g{}^4$
Sensible heat	$H_{g,b} = \rho C_p \frac{T_{g,b} - T_{air}}{r_{ah}}$	$H_{g,v} = \rho C_p \frac{T_{g,v} - T_{ac}}{r_{ah,g}}$	$H_v = 2(L_e + S_e)\rho C_p \frac{T_v - T_{ac}}{r_b}$
Latent heat	$LE_{g,b} = \frac{\rho C_p}{\gamma} \frac{e_{sat}\ (T_{g,b}) h_g - e_{air}}{r_{aw} + r_{soil}}$	$LE_{g,v} = \frac{\rho C_p}{\gamma} \frac{e_{sat}\ (T_{g,v}) h_g - e_{ac}}{r_{aw,g} + r_{soil}}$	$LE_v = \frac{\rho C_p}{\gamma}\left(C_e^w + C_t^w\right)\left(e_{sat}(T_v) - e_{ac}\right)$
Ground heat	$G_b = \frac{2\lambda_{isno+1}}{\Delta z_{isno+1}}\left(T_{g,b} - T_{isno+1}\right)$	$G_v = \frac{2\lambda_{isno+1}}{\Delta z_{isno+1}}\left(T_{g,v} - T_{isno+1}\right)$	

[a]The physical parameters and variables in the formulations:
$L_{air}\downarrow$ downward longwave radiation from the atmosphere (W m^{-2});
T_{air} air temperature (K) at a reference height;
e_{air} water vapor pressure (pa) at a reference height;
ε_g ground surface emissivity;
e_v vegetation emmisivity;
α_{gL} ground surface absorptivity for longwave radiation (= ε_g);
α_{vL} vegetation absorptivity for longwave (= ε_v);
σ Stefan-Boltzmann constant;
ρ air density (kg m^{-3});
C_p dry-air specific heat capacity (= 1005 J kg^{-1} K^{-1});
γ the psychrometric constant (= $\frac{C_p P_{air}}{0.622L}$, where P_{air} is the surface air pressure and L is latent heat of fusion ($T_{air} < 273.16$ K) or vaporization ($T_{air} < 273.16$ K);
h_g relative humidity of the air in the surface soil pore space (relative to the saturated vapor pressure at the water surface attached to soil particles);
T_{isno+1} temperature of the surface layer of snow (when $isno < 0$) or soil (when $isno = 0$);
λ_{isno+1} thermal conductivity of the surface layer of snow or soil;
Δz_{isno+1} layer thickness of the surface layer of snow or soil;
$L_v\downarrow$ downward longwave radiation reaching the ground including that transmitted through the canopy (= $(1-\alpha_{vL}) L_{air}\downarrow$ and emitted by the canopy (= $\varepsilon_v \sigma T_v{}^4$);
$L_g\uparrow$ upward longwave radiation from the ground including reflected (= $(1-\alpha_{gL}) L_v\downarrow$) and emitted by the ground ($\varepsilon_g \sigma T_g{}^4$);
T_{ac} temperature of the canopy air (can be derived from $H_{g,v} + H_v = \rho C_p\,(T_{ac} - T_{air})/r_{ah}$);
e_{ac} water vapor pressure of the canopy air (can be derived from $LE_{g,v} + LE_v = \frac{\rho C_p}{\gamma}\frac{e_{ac} - e_{air}}{r_{aw}}$);
$T_{g,b}$ ground surface temperature at the bare ground fraction;
$T_{g,v}$ ground surface temperature at the vegetated fraction;
T_v vegetation canopy surface temperature;
$e_{sat}(T_{g,b})$ saturated water vapor pressure (pa) at the temperature $T_{g,b}$;
$e_{sat}(T_{g,v})$ saturated water vapor pressure (pa) at the temperature $T_{g,v}$;
$e_{sat}(T_v)$ saturated water vapor pressure (pa) at the temperature T_v;
C_e^w $C_e^w = f_{wet}\,(L_e + S_e)/r_b$;
C_t^w $C_t^w = (1 - f_{wet})(L_{e,sun}/(r_b + r_{s,sun}) + L_{e,sha}/(r_b + r_{s,sha}))$;
L_e effective LAI (= LAI/F_{veg}), i.e., LAI converted to fractional vegetated area;
S_e effective stem area index (= SAI/F_{veg}), i.e., SAI converted to fractional vegetated area;
f_{wet} wet fraction of the canopy [*Deardorff*, 1978];
$L_{e,sun}$ effective sunlit LAI;
$L_{e,shd}$ effective shaded LAI;
r_{ah} aerodynamic resistance for heat (= $1/(C_H\,U_{air})$), where U_{air} is the wind speed at the reference height);
r_{aw} aerodynamic resistance for water vapor (= r_{ah});
$r_{ah,g}$ aerodynamic resistance below the canopy for heat [*Niu and Yang*, 2004];
$r_{aw,g}$ aerodynamic resistance below the canopy for water vapor (= $r_{ah,g}$);
r_{soil} soil surface resistance accounting for the resistance on water vapor transfer from the surface soil pore space to z_{0h} following *Sellers et al.* [1992];
$r_{s,sha}$ stomatal resistance per unit LAI of shaded leaves (see Appendix B);
$r_{s,sun}$ stomatal resistance per unit LAI of sunlit leaves (see Appendix B);
r_b leaf boundary layer resistance per unit LAI [*Brutsaert*, 1982].

the rate of photosynthesis per unit LAI of shaded and sunlit leaves, A_i (A_{shd} and A_{sun}), respectively,

$$\frac{1}{r_{s,i}} = m\frac{A_i}{c_{air}}\frac{e_{air}}{e_{sat}(T_v)}P_{air} + g_{\min} \tag{B1}$$

where c_{air} is the CO_2 concentration at leaf surface ($355 \times 10^{-6} \times P_{air}$ in the unit of pa), P_{air} surface air pressure (pa), e_{air} vapor pressure at the leaf surface (pa), $e_{sat}(T_v)$ saturation vapor pressure inside leaf (pa), $g_{\min}$ minimum stomatal conductance (μmolm^{-2}s^{-1}), m is an empirical parameter to relate transpiration with CO_2 flux (a larger m indicates the leaf consumes more water, i.e., greater transpiration, to produce the same carbon mass).

[68] The total carbon assimilation (or photosynthesis) rate (g m^{-2} s^{-1}),

$$A = 12 \times 10^{-6}(A_{sun}L_{sun} + A_{shd}L_{shd}) \tag{B2}$$

where A_{sun} and A_{shd} are photosynthesis rates (μmol m^{-2} s^{-1}) per unit LAI of sunlit and shaded leaves, and L_{sun} and L_{sha} are sunlit and shaded leaf area indices, respectively. L_{sun} and L_{sha} are respectively proportional to sunlit and shaded fractions of the canopy, which are computed from the two-stream radiation transfer scheme. The factor 12×10^{-6} is to transform the unit μmol m^{-2}s^{-1} to g m^{-2} s^{-1}.

$$A_i = I_{gs}\min\left(A_C, A_{L,i}, A_S\right) \quad i \text{ for sunlit and shaded leaves} \tag{B3}$$

where I_{gs} is a growing season index depending on leaf temperature, A_C, $A_{L,i}$, and A_S are carboxylase-limited (Rubisco-limited), light-limited, and export-limited (for C3 plants) photosynthesis rates per unit LAI, respectively [*Bonan*, 1996].

[69] A_C, $A_{L,i}$, and A_S are respectively,

$$A_c = \frac{(c_i - c_{cp})V_{\max}}{c_i + K_c(1 + o_i/K_o)} \tag{B4}$$

$$A_{L.i} = \frac{(c_i - c_{cp})4.6\alpha PAR_i}{c_i + 2c_{cp}} \tag{B5}$$

$$A_s = 0.5V_{\max} \tag{B6}$$

where c_i is the CO_2 concentration inside leaf cavity, which is about 0.7 times of the atmospheric CO_2 concentration, c_{air}, (pa), and o_i are the atmospheric O_2 concentration (pa). PAR_i (i for shaded and sunlit leaves) is photosynthetically active radiation (Wm^{-2}) per unit shaded and sunlit LAI. The factor 4.6 (μmol photons J^{-1}) is used to convert Wm^{-2} to μmol photons m^{-2} s^{-1}. c_{cp} is the CO_2 compensation point and equals to $0.5\frac{K_c}{K_o}0.21o_i$ (pa), where K_c and K_o are the Michaelis-Menton constants (pa) for CO_2 and O_2, respectively, varying with vegetation temperature T_v [*Collatz et al.*, 1991]. α is the quantum efficiency (μmol CO_2 per μmol photon).

[70] The maximum rate of carboxylation varies with temperature, foliage nitrogen, and soil water,

$$V_{\max} = V_{\max 25}a_{v\max}^{\frac{T_v-25}{10}}f(N)f(T_v)\beta \tag{B7}$$

where $V_{\max\ 25}$ is maximum carboxylation rate at 25°C (μmol CO_2 m^{-2} s^{-1}) and $\alpha_{v\max}$ is a temperature sensitive parameter. The $f(T_v)$ is a function that mimics thermal breakdown of metabolic processes [*Collatz et al.*, 1991]. The $f(N) \le 1$ is a foliage nitrogen factor, and $f(N) = 1$, in this study, assuming the foliage nitrogen is saturated. The β factor is the soil moisture controlling factor, as described by equations (12)–(14) in section 4.3.

[71] **Acknowledgments.** This work was funded by NASA grants NAG5–10209, NAG5–12577, NNX07A79G, NNX 08AJ84G, NNX09AJ48G, NOAA grant NA07OAR4310076, a KAUST grant, and National Natural Science Foundation of China Project 40828004. We thank Robert E. Dickinson for reading the manuscript.

References

Anderson, E. A. (1976), A point energy and mass balance model of a snow cover, *NOAA Tech. Rep. NWS 19*, 150 pp., Off. of Hydrol., Natl. Weather Serv., Silver Spring, Md.

Ball, J. T., I. E. Woodrow, and J. A. Berry (1987), A model predicting stomatal conductance and its contribution to the control of photosynthesis under different environmental conditions, in *Process in Photosynthesis Research*, vol. 1, edited by J. Biggins, pp. 221–234, Martinus Nijhoff, Dordrecht, Netherlands.

Betts, A. K., and J. H. Ball (1998), FIFE surface climate and site-average dataset 1987–89, *J. Atmos. Sci.*, *55*(7), 1091–1108, doi:10.1175/1520-0469(1998)055<1091:FSCASA>2.0.CO;2.

Beven, K. J., and M. J. Kirkby (1979), A physically based, variable contributing model of basin hydrology, *Hydrol. Sci. Bull.*, *24*, 43–69, doi:10.1080/02626667909491834.

Bonan, G. B. (1996), A land surface model (LSM version 1.0) for ecological, hydrological, and atmospheric studies: Technical description and user's guide, *NCAR Tech. Note NCAR/TN-417+STR*, 150 pp., Natl. Cent. for Atmos. Res., Boulder, Colo.

Bowling, L. C., et al. (2003), Simulation of high-latitude hydrologic responses in the Torne-Kalix Basin: PILPS Phase 2(e): 1. Experiment description and summary intercomparisons, *Global Planet. Change*, *38*, 1–30, doi:10.1016/S0921-8181(03)00003-1.

Brun, E., P. David, M. Sudul, and G. Brunot (1992), A numerical model to simulate snow cover stratigraphy for operational avalanche forecasting, *J. Glaciol.*, *38*(128), 13–22.

Brutsaert, W. A. (1982), *Evaporation Into the Atmosphere*, 299 pp., D. Reidel, Dordrecht, Netherlands.

Chen, J., and P. Kumar (2001), Topographic influence on the seasonal and inter-annual variation of water and energy balance of basins in North America, *J. Clim.*, *14*, 1989–2014, doi:10.1175/1520-0442(2001)014<1989:TIOTSA>2.0.CO;2.

Chen, F., K. E. Mitchell, J. Schaake, Y. Xue, H.-L. Pan, V. Koren, Q. Y. Duan, M. Ek, and A. Betts (1996), Modeling of land-surface evaporation by four schemes and comparison with FIFE observations, *J. Geophys. Res.*, *101*, 7251–7268, doi:10.1029/95JD02165.

Chen, F., Z. Janjic, and K. E. Mitchell (1997), Impact of atmospheric surface-layer parameterizations in the new land-surface scheme of the NCEP mesoscale Eta model, *Boundary Layer Meteorol.*, *85*, 391–421, doi:10.1023/A:1000531001463.

Chen, F., et al. (2007), Description and evaluation of the characteristics if the NCAR high-resolution land data assimilation system, *J. Appl. Meteorol. Climatol.*, *46*, 694–713, doi:10.1175/JAM2463.1.

Collatz, G. J., J. T. Ball, C. Grivet, and J. A. Berry (1991), Physiological and environmental regulation of stomatal conductance, photosynthesis and transpiration: A model that includes a laminar boundary layer, *Agric. For. Meteorol.*, *54*(2–4), 107–136.

Collatz, G. J., M. Ribascarbo, and J. A. Berry (1992), A coupled photosynthesis-stomatal conductance model for leaves of C4 plants, *Aust. J. Plant Physiol.*, *19*, 519–538, doi:10.1071/PP9920519.

Dai, Y., et al. (2003), The Common Land Model (CLM), *Bull. Am. Meteorol. Soc.*, *84*, 1013–1023, doi:10.1175/BAMS-84-8-1013.

Deardorff, J. W. (1978), Efficient prediction of ground surface temperature and moisture, with inclusion of a layer of vegetation, *J. Geophys. Res.*, *83*, 1889–1903, doi:10.1029/JC083iC04p01889.

Desborough, C. E. (1999), Surface energy balance complexity in GCM land surface models, *Clim. Dyn.*, *15*, 389–403, doi:10.1007/s003820050289.

Dickinson, R. E. (1983), Land surface processes and climate-surface albedos and energy balance, in *Theory of Climate*, *Adv. Geophys.*, vol. 25, edited by B. Saltzman, pp. 305–353, Academic, San Diego, Calif.

Dickinson, R. E., A. Henderson-Sellers, and P. J. Kennedy (1993), Biosphere-Atmosphere Transfer Scheme (BATS) version 1e as coupled to the NCAR Community Climate Model, *NCAR Tech. Note NCAR/TN-387+STR*, 80 pp., Natl. Cent. for Atmos. Res., Boulder, Colo.

Dickinson, R. E., M. Shaikh, R. Bryant, and L. Graumlich (1998), Interactive canopies for a climate model, *J. Clim.*, *11*, 2823–2836, doi:10.1175/1520-0442(1998)011<2823:ICFACM>2.0.CO;2.

Dickinson, R. E., et al. (2002), Nitrogen controls on climate model evapotranspiration, *J. Clim.*, *15*, 278–295, doi:10.1175/1520-0442(2002)015<0278:NCOCME>2.0.CO;2.

Dirmeyer, P. A., R. D. Koster, and Z. Guo (2006a), Do global models properly represent the feedback between land and atmosphere?, *J. Hydrometeorol.*, *7*, 1177–1198, doi:10.1175/JHM532.1.

Dirmeyer, P. A., X. Gao, M. Zhao, Z. Guo, T. Oki, and N. Hanasaki (2006b), GSWP-2: Multimodel analysis and implications for our perception of the land surface, *Bull. Am. Meteorol. Soc.*, *87*, 1381–1397, doi:10.1175/BAMS-87-10-1381.

Duan, Q., N. K. Ajami, X. Gao, and S. Sorooshian (2007), Multi-model ensemble hydrologic prediction using Bayesian model averaging, *Adv. Water Resour.*, *30*(5), 1371–1386, doi:10.1016/j.advwatres.2006.11.014.

Ek, M. B., K. E. Mitchell, Y. Lin, E. Rogers, P. Grunmann, V. Koren, G. Gayno, and J. D. Tarpley (2003), Implementation of Noah land surface model advancements in the National Centers for Environmental Prediction operational mesoscale Eta model, *J. Geophys. Res.*, *108*(D22), 8851, doi:10.1029/2002JD003296.

Entin, J. K., A. Robock, K. Y. Vinnikov, V. Zabelin, S. Liu, A. Namkhai, and T. Adyasuren (1999), Evaluation of Global Soil Wetness Project soil moisture simulations, *J. Meteorol. Soc. Jpn.*, *77*, 183–198.

Essery, R., J. Pomeroy, J. Parviainen, and P. Storck (2003), Sublimation of snow from coniferous forests in a climate model, *J. Clim.*, *16*, 1855–1864, doi:10.1175/1520-0442(2003)016<1855:SOSFCF>2.0.CO;2.

Famiglietti, J. S., and E. F. Wood (1994), Multiscale modeling of spatially variable water and energy balance processes, *Water Resour. Res.*, *30*(11), 3061–3078, doi:10.1029/94WR01498.

Fan, Y., G. Miguez-Macho, C. P. Weaver, R. Walko, and A. Robock (2007), Incorporating water table dynamics in climate modeling: 1.

Water table observation and equilibrium water table simulations, *J. Geophys. Res.*, *112*, D10125, doi:10.1029/2006JD008111.

Georgakakos, K. P., D.-J. Seo, H. Gupta, J. Schaake, and M. B. Butts (2004), Towards the characterization of streamflow simulation uncertainty through ensembles, *J. Hydrol.*, *298*, 222–241, doi:10.1016/j.jhydrol.2004.03.037.

Grell, G. A., and D. Dévényi (2002), A generalized approach to parameterizing convection combining ensemble and data assimilation techniques, *Geophys. Res. Lett.*, *29*(14), 1693, doi:10.1029/2002GL015311.

Gulden, L. E., Z.-L. Yang, and G.-Y. Niu (2007), Interannual variation in biogenic emissions on a regional scale, *J. Geophys. Res.*, *112*, D14103, doi:10.1029/2006JD008231.

Gulden, L. E., E. Rosero, Z.-L. Yang, T. Wagener, and G.-Y. Niu (2008), Model performance, model robustness, and model fitness scores: A new method for identifying good land-surface models, *Geophys. Res. Lett.*, *35*, L11404, doi:10.1029/2008GL033721.

Guo, Z. C., and P. A. Dirmeyer (2006), Evaluation of the Second Global Soil Wetness Project soil moisture simulations: 1. Intermodel comparison, *J. Geophys. Res.*, *111*, D22S02, doi:10.1029/2006JD007233.

Guo, Z. C., et al. (2006), GLACE: The Global Land-Atmosphere Coupling Experiment. Part II: Analysis, *J. Hydrometeorol.*, *7*, 611–625, doi:10.1175/JHM511.1.

Hedstrom, N. R., and J. W. Pomeroy (1998), Measurements and modeling of snow interception in the boreal forest, *Hydrol. Processes*, *12*, 1611–1625, doi:10.1002/(SICI)1099-1085(199808/09)12:10/11<1611::AID-HYP684>3.0.CO;2-4.

Jarvis, P. G. (1976), The interpretation of the variations in leaf water potential and stomatal conductance found in canopies in the field, *Philos. Trans. R. Soc. B*, *273*, 593–610, doi:10.1098/rstb.1976.0035.

Jiang, X., G.-Y. Niu, and Z.-L. Yang (2009), Impacts of vegetation and groundwater dynamics on warm season precipitation over the Central United States, *J. Geophys. Res.*, *114*, D06109, doi:10.1029/2008JD010756.

Jin, J. M., X. Gao, Z. L. Yang, R. C. Bales, S. Sorooshian, and R. E. Dickinson (1999), Comparative analyses of physically based snowmelt models for climate simulations, *J. Clim.*, *12*, 2643–2657, doi:10.1175/1520-0442(1999)012<2643:CAOPBS>2.0.CO;2.

Jordan, R. (1991), A one-dimensional temperature model for a snow cover, *Spec. Rep. 91–16*, Cold Reg. Res. and Eng. Lab., U.S. Army Corps of Eng., Hanover, N. H.

Kollet, S. J., and R. M. Maxwell (2008), Capturing the influence of groundwater dynamics on land surface processes using an integrated, distributed watershed model, *Water Resour. Res.*, *44*, W02402, doi:10.1029/2007WR006004.

Koren, V., J. C. Schaake, K. E. Mitchell, Q.-Y. Duan, F. Chen, and J. M. Baker (1999), A parameterization of snowpack and frozen ground intended for NCEP weather and climate models, *J. Geophys. Res.*, *104*, 19,569–19,585, doi:10.1029/1999JD900232.

Koster, R. D., and M. J. Suarez (1992), Modeling the land surface boundary in climate models as a composite of independent vegetation stands, *J. Geophys. Res.*, *97*, 2697–2715.

Koster, R. D., M. J. Suarez, A. Ducharne, M. Stieglitz, and P. Kumar (2000), A catchment-based approach to modeling land surface processes in a general circulation model: 1. Model structure, *J. Geophys. Res.*, *105*, 24,809–24,822, doi:10.1029/2000JD900327.

Koster, R. D., et al. (2004), Regions of strong coupling between soil moisture and precipitation, *Science*, *305*, 1138–1140, doi:10.1126/science.1100217.

Koster, R. D. et al. (2006), GLACE: The Global Land-Atmosphere Coupling Experiment. Part 1: Overview, *J. Hydrometeorol.*, *7*, 590–610, doi:10.1175/JHM510.1.

Liang, X., Z. Xie, and M. Huang (2003), A new parameterization for surface and groundwater interactions and its impact on water budgets with the variable infiltration capacity (VIC) land surface model, *J. Geophys. Res.*, *108*(D16), 8613, doi:10.1029/2002JD003090.

Liang, X. Z., M. Xu, K. E. Kunkel, G. A. Grell, and J. S. Kain (2007), Regional climate model simulation of U.S.–Mexico summer precipitation using the optimal ensemble of two cumulus parameterizations, *J. Clim.*, *20*, 5201–5207, doi:10.1175/JCLI4306.1.

Lindström, G., K. Bishop, and M. O. Löfvenius (2002), Soil frost and runoff at Svartberget, northern Sweden—Measurements and model analysis, *Hydrol. Processes*, *16*, 3379–3392, doi:10.1002/hyp.1106.

Livneh, B., Y. Xia, K. E. Mitchell, M. B. Ek, and D. P. Lettenmaier (2010), Noah LSM snow model diagnostics and enhancements, *J. Hydrometeorol.*, *11*, 721–738, doi:10.1175/2009JHM1174.1.

Lynch-Stieglitz, M. (1994), The development and validation of a simple snow model for GISS GCM, *J. Clim.*, *7*, 1842–1855, doi:10.1175/1520-0442(1994)007<1842:TDAVOA>2.0.CO;2.

Mahrt, L., and M. Ek (1984), The influence of atmospheric stability on potential evaporation, *J. Clim. Appl. Meteorol.*, *23*, 222–234, doi:10.1175/1520-0450(1984)023<0222:TIOASO>2.0.CO;2.

Mahrt, L., and H.-L. Pan (1984), A two-layer model of soil hydrology, *Boundary Layer Meteorol.*, *29*, 1–20, doi:10.1007/BF00119116.

Maxwell, R. M., and S. J. Kollet (2008), Interdependence of groundwater dynamics and land-energy feedbacks under climate change, *Nat. Geosci.*, *1*, 665–669, doi:10.1038/ngeo315.

Maxwell, R. M., and N. L. Miller (2005), Development of a coupled land surface and groundwater model, *J. Hydrometeorol.*, *6*, 233–247, doi:10.1175/JHM422.1.

Mitchell, K. E., et al. (2004), The multi-institution North American Land Data Assimilation System (NLDAS): Utilizing multiple GCIP products and partners in a continental distributed hydrological modeling system, *J. Geophys. Res.*, *109*, D07S90, doi:10.1029/2003JD003823.

Niu, G.-Y., and Z.-L. Yang (2004), The effects of canopy processes on snow surface energy and mass balances, *J. Geophys. Res.*, *109*, D23111, doi:10.1029/2004JD004884.

Niu, G.-Y., and Z.-L. Yang (2006), Effects of frozen soil on snowmelt runoff and soil water storage at a continental scale, *J. Hydrometeorol.*, *7*, 937–952, doi:10.1175/JHM538.1.

Niu, G.-Y., and Z.-L. Yang (2007), An observation-based formulation of snow cover fraction and its evaluation over large North American river basins, *J. Geophys. Res.*, *112*, D21101, doi:10.1029/2007JD008674.

Niu, G.-Y., Z.-L. Yang, R. E. Dickinson, and L. E. Gulden (2005), A simple TOPMODEL-based runoff parameterization (SIMTOP) for use in global climate models, *J. Geophys. Res.*, *110*, D21106, doi:10.1029/2005JD006111.

Niu, G.-Y., Z.-L. Yang, R. E. Dickinson, L. E. Gulden, and H. Su (2007), Development of a simple groundwater model for use in climate models and evaluation with Gravity Recovery and Climate Experiment data, *J. Geophys. Res.*, *112*, D07103, doi:10.1029/2006JD007522.

Oleson, K. W., et al. (2004), Technical description of the Community Land Model (CLM), *NCAR Tech. Note NCAR/TN-461+STR*, 174 pp., Natl. Cent. for Atmos. Res., Boulder, Colo. (Available at www.cgd.ucar.edu/tss/clm/distribution/clm3.0/index.html.)

Pan, H.-L., and L. Mahrt (1987), Interaction between soil hydrology and boundary layer development, *Boundary Layer Meteorol.*, *38*, 185–202, doi:10.1007/BF00121563.

Pan, M., et al. (2003), Snow process modeling in the North American Land Data Assimilation System (NLDAS): 2. Evaluation of model simulated snow water equivalent, *J. Geophys. Res.*, *108*(D22), 8850, doi:10.1029/2003JD003994.

Peters-Lidard, C. D., E. Blackburn, X. Liang, and E. F. Wood (1998), The effect of soil thermal conductivity parameterization on surface energy fluxes and temperatures, *J. Atmos. Sci.*, *55*(7), 1209–1224, doi:10.1175/1520-0469(1998)055<1209:TEOSTC>2.0.CO;2.

Pielke, R. A., G. E. Liston, J. L. Eastman, L. Lu, and M. Coughenour (1999), Seasonal weather prediction as an initial value problem, *J. Geophys. Res.*, *104*, 19,463–19,479, doi:10.1029/1999JD900231.

Pitman, A. J. (2003), The evolution of, and revolution in, land surface schemes designed for climate models, *Int. J. Climatol.*, *23*, 479–510, doi:10.1002/joc.893.

Pitman, A. J., Y. Xia, M. Leplastrier, and A. Henderson-Sellers (2003), The CHAmeleon Surface Model: Description and use with the PILPS phase 2 (e) forcing data, *Global Planet. Change*, *38*, 121–135, doi:10.1016/S0921-8181(03)00015-8.

Roesch, A., M. Wild, H. Gilgen, and A. Ohmura (2001), A new snow cover fraction parameterization for ECHAM4 GCM, *Clim. Dyn.*, *17*, 933–946, doi:10.1007/s003820100153.

Rosero, E., Z.-L. Yang, L. E. Gulden, G.-Y. Niu, and D. J. Gochis (2009), Evaluating enhanced hydrological representations in Noah-LSM over transition zones: Implications for model development, *J. Hydrometeorol.*, *10*, 600–622, doi:10.1175/2009JHM1029.1.

Schaake, J. C., V. I. Koren, Q.-Y. Duan, K. E. Mitchell, and F. Chen (1996), Simple water balance model for estimating runoff at different spatial and temporal scales, *J. Geophys. Res.*, *101*, 7461–7475, doi:10.1029/95JD02892.

Schlosser, C. A., and P. C. D. Milly (2002), A model-based investigation of soil moisture predictability and associated climate predictability, *J. Hydrometeorol.*, *3*, 483–501, doi:10.1175/1525-7541(2002)003<0483:AMBIOS>2.0.CO;2.

Sellers, P. J. (1985), Canopy reflectance, photosynthesis and transpiration, *Int. J. Remote Sens.*, *6*, 1335–1372, doi:10.1080/01431168508948283.

Sellers, P. J., M. D. Heiser, and F. G. Hall (1992), Relations between surface conductance and spectral vegetation indices at intermediate (100 m^2 to 15 km^2) length scales, *J. Geophys. Res.*, *97*, 19,033–19,059, doi:10.1029/92JD01096.

Sellers, P. J., D. A. Randall, G. J. Collatz, J. A. Berry, C. B. Field, D. A. Dazlich, C. Zhang, G. D. Collelo, and L. Bounoua (1996), A revised land surface parameterization (SiB2) for atmospheric GCMs: Part I. Model formulation, *J. Clim.*, *9*, 676–705, doi:10.1175/1520-0442(1996)009<0676:ARLSPF>2.0.CO;2.

Sellers, P. J., et al. (1997), Modeling the exchanges of energy, water, and carbon between continents and the atmosphere, *Science*, *275*(5299), 502–509, doi:10.1126/science.275.5299.502.

Shanley, J. B., and A. Chalmers (1999), The effect of frozen soil on snowmelt runoff at Sleepers River, Vermont, *Hydrol. Processes*, *13*, 1843–1857, doi:10.1002/(SICI)1099-1085(199909)13:12/13<1843::AID-HYP879>3.0.CO;2-G.

Sivapalan, M., K. Beven, and E. F. Wood (1987), On hydrologic similarity: 2. A scaled model of storm runoff production, *Water Resour. Res.*, *23*(12), 2266–2278, doi:10.1029/WR023i012p02266.

Slater, A. G., T. J. Bohn, J. L. McCreight, M. C. Serreze, and D. P. Lettenmaier (2007), A multimodel simulation of pan-Arctic hydrology, *J. Geophys. Res.*, *112*, G04S45, doi:10.1029/2006JG000303.

Stieglitz, M., D. Rind, J. Famiglietti, and C. Rosenzweig (1997), An efficient approach to modeling the topographic control of surface hydrology for regional and global modeling, *J. Clim.*, *10*, 118–137, doi:10.1175/1520-0442(1997)010<0118:AEATMT>2.0.CO;2.

Sun, S. F., J. M. Jin, and Y. Xue (1999), A simple snow-atmosphere-soil transfer model, *J. Geophys. Res.*, *104*, 19,587–19,597, doi:10.1029/1999JD900305.

Verseghy, D. L. (1991), CLASS-A Canadian land surface scheme for GCMS: I. Soil model, *Int. J. Climatol.*, *11*, 111–133, doi:10.1002/joc.3370110202.

Wolock, D. M., and G. J. McCabe (2000), Differences in topographic characteristics computed from 100- and 1000-m resolution digital elevation model data, *Hydrol. Processes*, *14*, 987–1002, doi:10.1002/(SICI)1099-1085(20000430)14:6<987::AID-HYP980>3.0.CO;2-A.

Xue, Y., P. J. Sellers, J. L. Kinter, and J. Shukla (1991), A simplified biosphere model for global climate studies, *J. Clim.*, *4*, 345–364, doi:10.1175/1520-0442(1991)004<0345:ASBMFG>2.0.CO;2.

Xue, Y., S. Sun, D. S. Kahan, and Y. Jiao (2003), Impact of parameterizations in snow physics and interface processes on the simulation of snow cover and runoff at several cold region sites, *J. Geophys. Res.*, *108*(D22), 8859, doi:10.1029/2002JD003174.

Yang, Z.-L. (2004), Modeling land surface processes in short-term weather and climate studies, in *Observation, Theory and Modeling of Atmospheric Variability*, *World Sci. Ser. Asia-Pac. Weather Clim.*, vol. 3, edited by X. Zhu et al., pp. 288–313, World Sci., River Edge, N. J., doi:10.1142/9789812791139_0014.

Yang, Z.-L., and R. E. Dickinson (1996), Description of the Biosphere-Atmosphere Transfer Scheme (BATS) for the soil moisture workshop and evaluation of its performance, *Global Planet. Change*, *13*, 117–134, doi:10.1016/0921-8181(95)00041-0.

Yang, R., and M. A. Friedl (2003), Modeling the effects of three-dimensional vegetation structure on surface radiation and energy balance in boreal forests, *J. Geophys. Res.*, *108*(D16), 8615, doi:10.1029/2002JD003109.

Yang, Z.-L., and G.-Y. Niu (2003), The versatile integrator of surface and atmosphere processes (VISA) part I: Model description, *Global Planet. Change*, *38*, 175–189, doi:10.1016/S0921-8181(03)00028-6.

Yang, Z.-L., R. E. Dickinson, A. Robock, and K. Y. Vinnikov (1997), Validation of the snow sub-model of the Biosphere-Atmosphere Transfer Scheme with Russian snow cover and meteorological observational data, *J. Clim.*, *10*, 353–373, doi:10.1175/1520-0442(1997)010<0353:VOTSSO>2.0.CO;2.

Yang, Z.-L., G.-Y. Niu, K. E. Mitchell, F. Chen, M. B. Ek, M. Barlage, K. Manning, D. Niyogi, M. Tewari, and Y.-L. Xia (2011), The community Noah land surface model with multiparameterization options (Noah-MP): 2. Evaluation over global river basins, *J. Geophys. Res.*, *116*, D12110, doi:10.1029/2010JD015140.

Yeh, P. J.-F., and E. A. B. Eltahir (2005), Representation of water table dynamics in a land surface scheme. Part I: Model development, *J. Clim.*, *18*, 1861–1880, doi:10.1175/JCLI3330.1.

M. Barlage, F. Chen, K. Manning, and M. Tewari, Research Applications Laboratory, National Center for Atmospheric Research, Boulder, CO 80307, USA.

M. B. Ek, K. E. Mitchell, and Y. Xia, Environmental Modeling Center, National Centers for Environmental Prediction, National Oceanic and Atmospheric Administration-National Weather Service, 5200 Auth Rd., Camp Springs, MD 20746, USA.

A. Kumar, Hydrological Science Branch, NASA Goddard Space Flight Center, Greenbelt, MD 20771, USA.

G.-Y. Niu, Biosphere 2, University of Arizona, Tucson, AZ 85738, USA.

D. Niyogi, Department of Agronomy, Purdue University, West Lafayette, IN 47907, USA.

E. Rosero, ExxonMobil Upstream Research Company, Houston, TX 77098, USA.

Z.-L. Yang, Department of Geological Sciences, 1 University Station C1100, University of Texas at Austin, Austin, TX 78712, USA. (liang@jsg.utexas.edu)